Effects of Singular-Vector-Type Initial Errors on the Short-Range Prediction of Kuroshio Extension Transition Processes

QIANG WANG

Key Laboratory of Ocean Circulation and Waves, Institute of Oceanology, Chinese Academy of Sciences, Qingdao, China, and Environmental Science and Engineering, University of Northern British Columbia, Prince George, British Columbia, Canada, and Qingdao National Laboratory for Marine Science and Technology, Qingdao, China

YOUMIN TANG

Environmental Science and Engineering, University of Northern British Columbia, Prince George, British Columbia, Canada, and State Key Laboratory of Satellite Ocean Environment Dynamics, Second Institute of Oceanography, Hangzhou, China

STEFANO PIERINI

Dipartimento di Scienze e Tecnologie, Università di Napoli Parthenope, Naples, and CoNISMa, Rome, Italy

MU MU

Key Laboratory of Ocean Circulation and Waves, Institute of Oceanology, Chinese Academy of Sciences, and Qingdao National Laboratory for Marine Science and Technology, Qingdao, China

(Manuscript received 12 April 2016, in final form 5 April 2017)

ABSTRACT

The effects of optimal initial error on the short-range prediction of transition processes between the Kuroshio Extension (KE) bimodalities are analyzed using a reduced-gravity shallow-water model and the singular vector (SV) approach. Emphasis is placed on the spatial structures, growing processes, and effects of the SVs. The results show that the large values of the SVs are mainly located in the first crest region of the KE (around 35°N, 144°E) and in the Kuroshio large meander (KLM) region south of Japan (around 32°N, 139.5°E). The fast growths of the SVs have important impacts on the prediction of transition of the KE bimodality. The initial error with +SV pattern (with positive anomalies in the first crest region of the KE and negative anomalies in the KLM region) tends to strengthen the KE and shift it toward the high-energy state, while the error with −SV pattern is prone to weaken the KE and shift it toward the low-energy state. In addition, the SV-type initial errors grow more quickly in the transition phase of the KE from the high-energy to the low-energy state than in the opposite transition phase. A perturbation energy analysis illustrates that different physical processes are responsible for the error growth in the KE region for different transition phases of the KE; barotropic instability plays a dominant role in the error growth in the low-to-high (LH) energy phase, while the error evolution in the high-to-low (HL) energy phase is mainly caused by advection processes.

1. Introduction

The Kuroshio Extension (KE) is a strong eastward inertial meandering jet originating from the east coastline of Japan and formed by the confluence of the Kuroshio and Oyashio western boundary currents of the North Pacific wind-driven subtropical and subpolar gyres, respectively (e.g., Qiu 2002). Qiu and Chen (2005, 2010) showed that the KE exhibits a distinctive low-frequency variability (LFV) of bimodal character on the decadal time scale, which exhibits transitions between a highly energetic elongated state (characterized by two stable anticyclonic meanders known as "crests" between 140° and 152°E and by a strong southern recirculation gyre) and a weaker, more convoluted and variable, and less zonally elongated contracted state.

That KE LFV has important effects on the weather, climate, and fisheries. For example, Qiu (2000) and Seager et al. (2001) pointed out that variations of the KE state can bring about strong sea surface temperature

Corresponding author: Prof. Youmin Tang, ytang@unbc.ca

DOI: 10.1175/JCLI-D-16-0305.1

(SST) anomalies. Some studies found that these SST anomalies in the KE region have significant effects on the Pacific storm tracks, the development of clouds, the atmospheric transient eddy heat fluxes in the Northern Hemisphere winter, and the large-scale atmosphere circulation (O'Reilly and Czaja 2015; Tokinaga et al. 2009; Frankignoul et al. 2011; Kwon and Joyce 2013). In addition, Nishikawa et al. (2011) found that the survival rate of Japanese sardines has a significant correlation with the variabilities of SST and mixed layer depth in the KE region. Because of these influences, the dynamics and predictability studies of the KE LFV have attracted the attention of many researchers (e.g., Qiu 2003; Qiu and Chen 2005, 2010; Kelly et al. 2010; Nonaka et al. 2012, 2016).

Different dynamical mechanisms potentially responsible for the KE LFV have been investigated. Qiu and Chen (2005) showed that the KE LFV cannot be explained as a direct response to atmospheric fluctuations, which is not surprising since the KE jet is highly nonlinear. Hence, the intrinsic oceanic mechanisms are expected to play a dominant role. Nonetheless, the atmospheric variability does play an important role: by analyzing the sea surface height (SSH) signal derived from satellite altimetric data, Qiu and Chen (2005, 2010) showed that westward-propagating Rossby wave anomalies generated in the eastern North Pacific by the wind stress anomalies at different phases of the Pacific decadal oscillation are in synchrony with the low-frequency positional shifts of the KE. This apparent paradox can be resolved by considering the KE decadal cycle as a case of intrinsic oceanic variability excited, and therefore paced, by the atmospheric forcing (Pierini 2014).

The above-mentioned intrinsic oceanic mechanisms have been explored in several modeling studies both in the context of the double-gyre problem of the wind-driven ocean circulation with different degrees of idealizations (e.g., Dijkstra and Ghil 2005; Schmeits and Dijkstra 2001; Pierini 2006) and with high-resolution ocean general circulation models (OGCMs; e.g., Taguchi et al. 2007, 2010; Nonaka et al. 2006, 2012; Douglass et al. 2012; Kurogi et al. 2013). It is worth mentioning that Pierini (2006) and Pierini et al. (2009) used a 1.5-layer reduced-gravity shallow-water model of the North Pacific with a steady wind stress forcing to simulate the LFV of the KE. Despite the relatively idealized setting of the model study, the main features of the modeled LFV correspond fairly well with those determined from observations. Although no general consensus has been reached on the detailed dynamical mechanisms that lead to the KE LFV, these model studies provide useful guidance for the simulation and prediction of the phenomenon.

Although no operational forecast has been developed for the KE LFV, predictability studies have been carried out [e.g., Nonaka et al. 2012; Kramer et al. 2012; Qiu et al. 2014; see Pierini et al. (2014) for a review]. By considering the wind-forcing mechanism mentioned above, Nonaka et al. (2012) estimated the predictability time for the transitions between the KE states by correlation analysis: they showed that the SSH anomalies in the eastern North Pacific resulting from wind stress anomalies will take about three years to propagate to the KE region. Therefore, they suggested that the transitions of the KE states could be predicted three years in advance. Qiu et al. (2014) considered the coupling between the KE and atmosphere and found that the predictive time limit is 4–6 years.

In predictability studies of frontal-scale fluctuations such as the KE LFV, consideration of the oceanic intrinsic instabilities is very important. In fact, those instabilities may cause the rapid growth of an initial error in a short term, which will influence the results of the numerical prediction. In the predictability study of the weather and climate, the initial error growth has been investigated using various approaches (e.g., Farrell 1990; Simmons et al. 1995; Mu et al. 2007), among which the singular vector (SV) method is widely used. For the predictability of ocean currents, the SV method has been used to explore the optimal error growths in the prediction of the Gulf Stream state (Moore and Mariano 1999) and the Kuroshio large meander (KLM) south of Japan (Fujii et al. 2008). As Ehrendorfer and Tribbia (1997) pointed out, for numerical forecasts, sampling the fastest growing errors among all possible initial errors is most important. The SV approach can in fact determine this kind of initial error that grows most rapidly under the assumption that the growth is linear in time.

In this context, we will employ the SV method to explore the effects of the initial SSH error on the prediction of the transition of the KE states in the shallow-water model developed by Pierini (2006), which is able to capture some relevant observational features of the KE variations. Taking into account that the corresponding adjoint model is not available, we will utilize an adjoint-free ensemble-based strategy introduced by Kleeman et al. (2003) to calculate the SV. This strategy has also been applied to some realistic climate models to obtain the climatically relevant SV (Tang et al. 2006; Hawkins and Sutton 2011; Islam et al. 2016). Moreover, we will analyze the spatial structure characteristic of the optimal initial error obtained through the SV method and its growing processes to reveal the dynamical mechanism of the error growth. This study will contribute to providing effective strategies for developing the ensemble prediction system of the KE and useful guidance for improving the prediction skills of the KE.

The paper is organized as follows. In section 2, the numerical model and the SV method are introduced. The leading SV and its robustness are discussed in section 3. In section 4 the evolution processes of the leading SV are investigated. Finally, in section 5 conclusions are drawn.

2. Model and method

a. The shallow-water model

In this study, we use the 1.5-layer reduced-gravity shallow-water model of Pierini (2006) to simulate the KE LFV. The same model has been extended to investigate the roles of North Pacific Ocean basin geometry, stochastic winds, and time-dependent North Pacific Oscillation (NPO) wind forcing in the simulation of the KE LFV (Pierini 2008, 2010, 2014). The effects of the ocean observations on the prediction of the KE state have been analyzed by Kramer et al. (2012) with the same modeling tool.

Despite the relative simplicity of this KE model, its performance is good in many respects: see section 3 of Pierini (2006) for the validation of the modeled mean jet with climatological data and sections 4a and 4b of the same article and section 2b of Pierini et al. (2009) for the validation of the modeled KE decadal variability with altimetric data. In those studies the limits of the model are acknowledged and discussed, but it is significant that such a model can nonetheless produce relatively realistic intrinsic KE cycles thanks to the inclusion of essential elements of realism in the model implementation. KE models that should in principle be more realistic yield less realistic KE cycles, or they do not yield them at all. For an explanation, see section 3 of Pierini (2014) and section 2 of Pierini (2015) for a detailed analysis of the modeling problems that can explain such an apparently paradoxical situation.

Although baroclinic instability is known to play a major role in the dynamics of the Kuroshio Current south of Japan (e.g., Miyazawa et al. 2004; Tsujino et al. 2006; Usui et al. 2008), the good performance of our model (that does not include baroclinic instability processes) in the KE LFV suggests that barotropic instability is likely to play a major role in the KE jet transitions. The recent work of Wang et al. (2016) based on altimetric and Argo data support the conclusion that baroclinic instability is not the dominant mechanism influencing the decadal modulation of the mesoscale eddy field in the KE region, while barotropic instability is found to make an important contribution to the decadal modulation.

The ocean model used here is, therefore, a valuable tool to analyze basic aspects of the KE LFV and, thanks to its limited computational cost compared to OGCMs, is particularly suitable for implementing the complex mathematical procedure developed in the present study to investigate the effects of singular-vector-type initial errors on the short-range prediction of the KE.

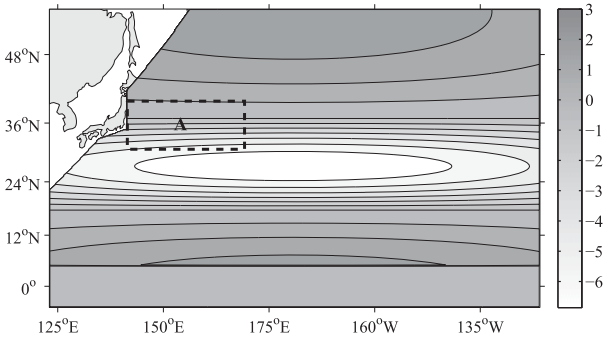

FIG. 1. The model domain (5°S–55°N, 122°E–120°W) and climatological wind stress curl ($\times 10^{-8}\,\mathrm{N\,m^{-3}}$) used in the simulations. The area A denotes the KE region.

We now briefly describe the ocean model [for any other details see Pierini (2006)]. The ocean is assumed to consist of a single active layer superimposed on an infinitely deep and quiescent lower layer. The ocean dynamics is thus governed by the following reduced-gravity shallow-water equations:

$$\frac{\partial u}{\partial t}+u\frac{\partial u}{\partial x}+v\frac{\partial u}{\partial y}-fv=-g'\frac{\partial \eta}{\partial x}+A_H\nabla^2 u - \gamma u\sqrt{u^2+v^2}+\frac{\tau}{\rho h}, \tag{1a}$$

$$\frac{\partial v}{\partial t}+u\frac{\partial v}{\partial x}+v\frac{\partial v}{\partial y}+fu=-g'\frac{\partial \eta}{\partial y}+A_H\nabla^2 v - \gamma v\sqrt{u^2+v^2}, \quad \text{and} \tag{1b}$$

$$\frac{\partial \eta}{\partial t}+\frac{\partial (hu)}{\partial x}+\frac{\partial (hv)}{\partial y}=0, \tag{1c}$$

where u and v are the zonal and meridional velocity components, respectively, $h = D + \eta$ is the upper-layer thickness, where $D = 500\,\mathrm{m}$ is the undisturbed layer thickness and η is the interface displacement (positive downward), $\tau(x)$ is the wind stress, $A_H = 220\,\mathrm{m^2\,s^{-1}}$ and $\gamma = 5\times10^{-4}\,\mathrm{m^{-1}}$ are the lateral eddy viscosity and interfacial friction coefficients, respectively, $g' = g\Delta\rho/\rho = 0.045\,\mathrm{m\,s^{-2}}$ is the reduced gravity, $\Delta\rho/\rho$ is the relative variation of density between the two layers, and f is the Coriolis parameter.

To simulate the KE, the model domain is set as a part of the Pacific basin (5°S–55°N, 122°E–120°W) with a schematic coastline in the western boundary, as shown in Fig. 1 [the importance of these geometric features has been discussed in Pierini (2008)]. The spatial resolution

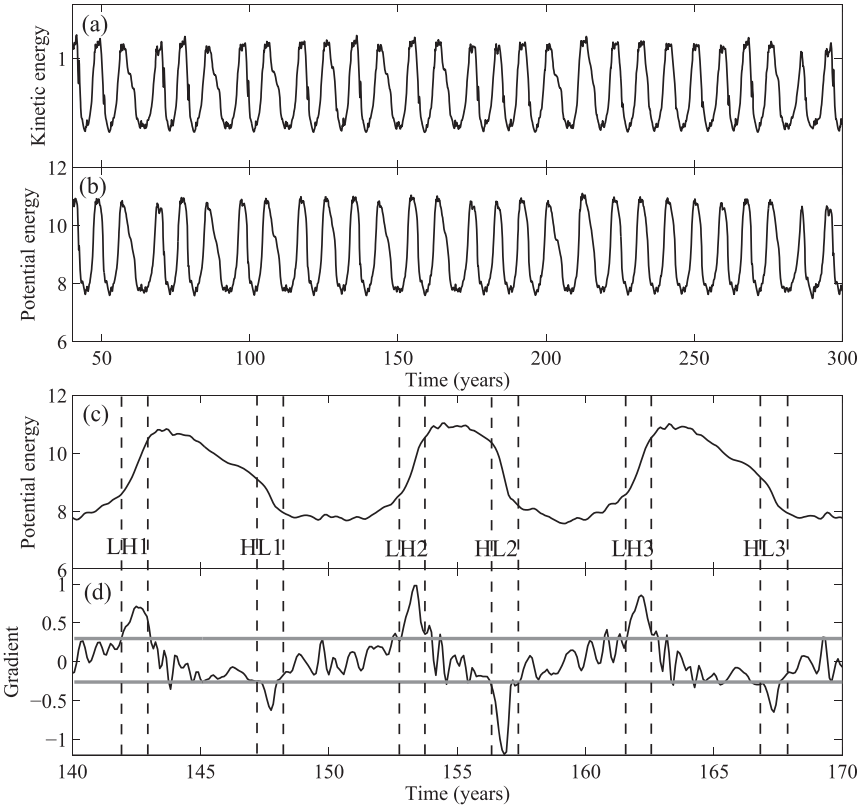

FIG. 2. Time series of the monthly averaged (a) kinetic energy and (b) potential energy ($10^{13}\,m^5\,s^{-2}$) integrated over the KE region A (Fig. 1) using Eq. (3). The correlation coefficient between these two time series is 0.99. (c) The enlargement of the time series of the potential energy in (b) and (d) the time series of the tendency of the potential energy ($10^6\,m^5\,s^{-3}$), both for the years 140–170. The vertical dashed lines denote the start and end points of each chosen transition process. The two gray lines in (d) correspond to the tendencies 0.3 and $-0.26 \times 10^6\,m^5\,s^{-3}$, respectively.

is $\Delta x = \Delta y = 20$ km and the time step is 20 min. The flow is driven by a steady zonal wind stress field (its curl is shown in Fig. 1), which is an analytical approximation of the climatological zonal wind field. The SSH $\tilde{\eta}$ (positive upward) is obtained from the following relation:

$$\tilde{\eta} \cong \eta\Delta\rho/\rho. \tag{2}$$

Further details can be found in Pierini (2006).

The model is integrated for 300 yr from vanishing initial conditions. The first 40 yr are discarded because they belong to the spinup phase, so the subsequent 260 yr are used in the following analysis. Following Pierini (2006), to characterize the different dynamical states of the KE, the kinetic and potential energy in the KE region denoted as A (Fig. 1) are used:

$$E_K(t) = \frac{1}{2}\iint_A h(u^2 + v^2)\,dx\,dy; \quad E_P(t) = \frac{1}{2}g'\iint_A \eta^2\,dx\,dy. \tag{3}$$

It should be stressed that the kinetic energy $E_K(t)$ refers to the total kinetic energy rather than the eddy kinetic energy. Figures 2a and 2b show the time series of the monthly averaged kinetic energy and potential energy. The two time series are very similar with a correlation coefficient of 0.99, and both exhibit the typical decadal changes of the modeled KE, indicating that the two series can both represent the KE LFV. Pierini (2006) showed that the high-energy state corresponds to the elongated state of the KE, while the low-energy state corresponds to the contracted state, which is consistent with the result derived from SSH observations by Qiu (2003). In addition, as already pointed out, Pierini et al. (2009) have compared the simulations obtained by the current model and the observational SSH data and confirmed that the modeled KE bimodal cycle agrees well with the observed one. This motivates us to investigate the predictability of the transition of the KE states using this model. Notice that, for the sake of

simplicity, the modeled bimodal states of the KE are labeled as high- and low-energy states in the following discussion.

b. Singular vector method

In this subsection, we will recall the SV method (e.g., Buizza and Palmer 1995; Kleeman et al. 2003). A general dynamical system can be written formally as

$$\mathbf{X}(t+\Delta t)=\mathbf{M}[\mathbf{X}(t)], \tag{4}$$

where $\mathbf{X}$ is the state vector of the system and $\mathbf{M}$ is a nonlinear propagator. If there exists a "small" error $\mathbf{x}$ at time t, Eq. (4) becomes

$$\mathbf{X}(t+\Delta t)+\mathbf{x}(t+\Delta t)=\mathbf{M}[\mathbf{X}(t)+\mathbf{x}(t)], \tag{5}$$

where $\mathbf{x}(t+\Delta t)$ denotes the evolution of the error $\mathbf{x}(t)$. Subtracting Eq. (4) from Eq. (5), the evolution of the error can be approximated by the following linear equation:

$$\mathbf{x}(t+\Delta t)=\mathbf{L}\mathbf{x}(t), \tag{6}$$

where $\mathbf{L}$ is the tangent linear approximation of the nonlinear propagator $\mathbf{M}$ at time t with the expression $\mathbf{L}=\partial\mathbf{M}[\mathbf{X}(t)]/\partial\mathbf{X}$. For the linear system in Eq. (6), the SV approach is to find the error that grows fastest among all the errors with the same magnitude during the interval Δt. The SV can then be obtained by calculating the eigenvectors of $\mathbf{L}^{\mathrm{T}}\mathbf{L}$, where the superscript T denotes the transpose.

In general, to obtain the SV, the tangent and adjoint models of the original forward numerical model need to be developed, but this is very difficult, or even intractable, for complicated oceanic and atmospheric models. In addition, for seasonal or longer time scale predictions, it is important to filter out small-scale noise while retaining large-scale processes. To address these issues, we adopt the ensemble-based strategy proposed by Kleeman et al. (2003) to calculate the SV. The procedure of this strategy is summarized in the following eight steps:

1) Choose the variables that are perturbed at the initial time. In our reduced-gravity shallow-water model, a streamfunction can be defined by the SSH $\tilde{\eta}$ [i.e., $\varphi=(g/f)\tilde{\eta}$]. The velocities u and v can thus be approximated by the spatial derivatives of $\tilde{\eta}$ (the Ekman component of flow velocity is assumed negligible), according to $u=-\partial\varphi/\partial y$ and $v=-\partial\varphi/\partial x$. Thus, when the SSH field is perturbed, the velocity perturbation can be easily obtained during the adjustment of the SSH perturbation. Therefore, we only perturb the SSH $\tilde{\eta}$ [or η according to Eq. (2)].
2) Calculate the leading five empirical orthogonal function (EOF) modes of the SSH anomaly field. The last 260-yr monthly mean SSH anomaly data from the 300-yr control integration of the model are used to compute the five EOFs, which are shown in Fig. 3. The first EOF is an LFV mode of the KE associated with the variability of the Kuroshio south of Japan and explains 51% of the total variance. The second EOF is a variability mode of the Kuroshio south of Japan with 22.8% explained variance. The third, fourth, and fifth EOF modes represent the mesoscale or higher-frequency variations in the KE region with a small explained variance. Here we use the covariance EOFs rather than the correlation EOFs used by Kleeman et al. (2003) because the SV derived from the correlation EOFs exhibits small-scale structures (not shown) having no significant effects on the prediction of the KE.
3) Choose the background states from the control integration. This study mainly focuses on the transitions between the KE bimodalities. For the sake of simplicity, we denote the transition from the low- to the high-energy state as the low-to-high (LH) energy phase and the opposite as the HL phase. To define the transition phases of the KE bimodality, we show the time series of the potential energy for 140–170 yr and its tendency in Figs. 2c and 2d. When the KE is in any of the two (high or low energy) states, the absolute value of the tendency is small; on the contrary, when the KE is in a transition phase, the absolute value attains a relative maximum. Hence, the KE transition periods are defined as those in which the absolute value of the tendency of the potential energy is large. More precisely, the LH energy phase occurs when the tendency of the potential energy is greater than $0.3\times10^{6}\,\mathrm{m^{5}\,s^{-3}}$, while the high-to-low (HL) energy phase occurs when the tendency is less than $-0.26\times10^{6}\,\mathrm{m^{5}\,s^{-3}}$ (see the two horizontal lines in Fig. 2d). To confirm that the above criteria can actually identify the KE transition phases, we also examine the spatial structures of the SSH field in the KE region. Since the transition processes are similar for the same transition phase, we show the SSH map for the two transition processes LH1 and HL1 in Fig. 4. For LH1 (Figs. 4a–c), the KE starts with a low-energy state at the initial time characterized by a weak crest around (35°N, 143°E); subsequently, the crest becomes stronger as the KE transits toward the high-energy state. The opposite process can be seen in Figs. 4d–f for HL1: now the KE shifts from the high-energy state to a low-energy state. Naturally, the two transitions are asymmetrical in the model (see Pierini 2006), as in SSH observations. According

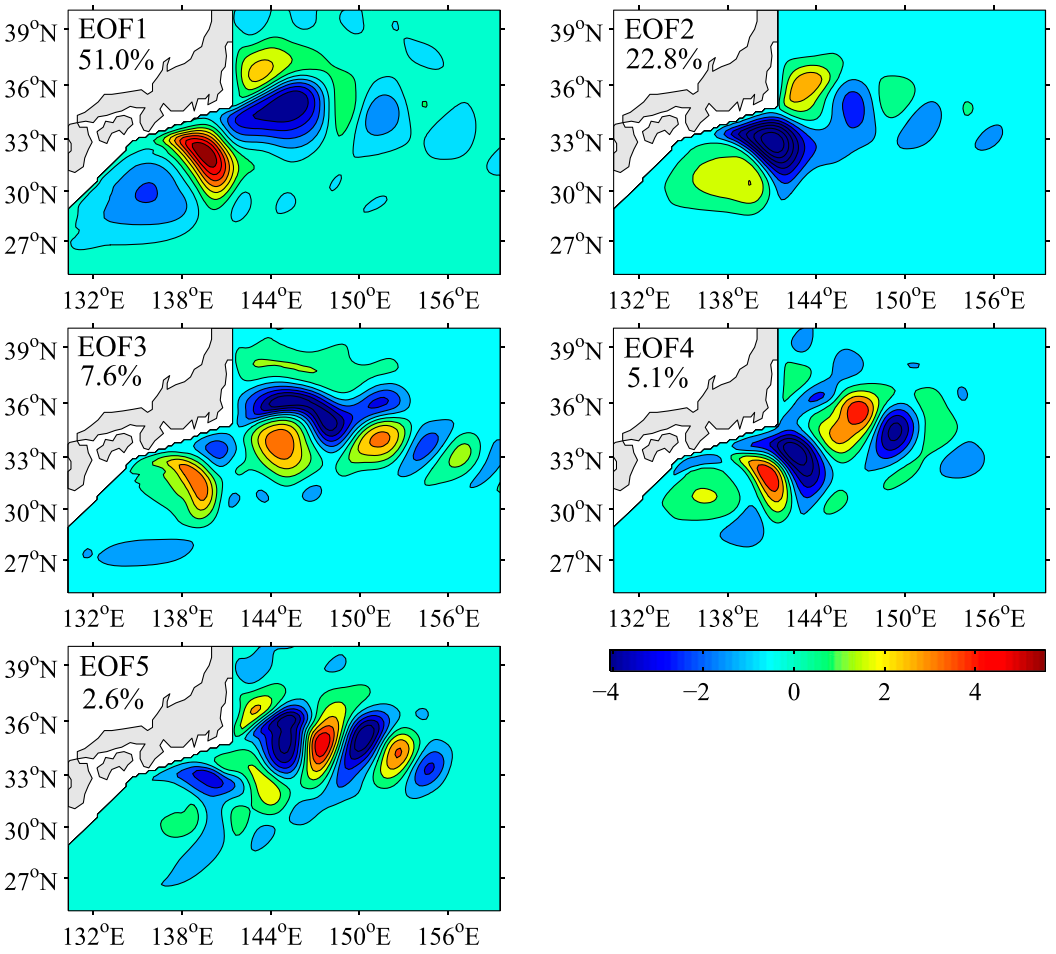

FIG. 3. The leading five EOF modes of the monthly mean SSH anomaly field (cm). The explained variance (%) for each EOF mode is reported in each panel.

to the criteria each transition phase of the KE has a period of ~1 yr, which can also be seen from Fig. 2d.

In the following, we choose six transition processes to determine the background states: three for the LH phase (denoted by LH1, LH2, and LH3) and three for the HL phase (denoted by HL1, HL2, and HL3). These are shown in Fig. 2d (vertical dashed lines). Each LH transition process begins when the tendency is close to $0.3 \times 10^6\,\mathrm{m^5\,s^{-3}}$, while for HL each transition process begins when the tendency is close to $-0.26 \times 10^6\,\mathrm{m^5\,s^{-3}}$. The accurate starting time for each transition process is listed in Table 1. Furthermore, for convenience the period for each process is always taken as 360 days, which approximately corresponds to the period of the KE transition phase. Based on this choice, it should be noted that, since differences exist between any two transitions (even for the same phase) due to the chaotic nature of the flow (Pierini 2006), the tendencies of the final points are only around $0.3 \times 10^6\,\mathrm{m^5\,s^{-3}}$ for the LH phase and $-0.26 \times 10^6\,\mathrm{m^5\,s^{-3}}$ for the HL phase, but not exactly equal to them, as shown in Fig. 2d. Also, it is worth pointing out that the potential energy of the starting point for HL2 is greater than those for HL1 and HL3 (Fig. 2c). The reason is that the KE undergoes faster transition in HL2 as shown by the larger tendency in Fig. 2d. It should also be noted that although the starting points are different, the potential energies of the final points for HL1, HL2, and HL3 are basically the same (Fig. 2c).

In this study, we mainly focus on the effects of initial error growth on the short-range prediction of the KE transition process. So the lead time is taken as 180 days. This choice is based on the following consideration: the linear approximation is valid during 180 days (see section 3b), which is a precondition for applying the SV approach. We also tested the validity of the linear approximation for a longer lead time such as 360 days and found that the approximation becomes invalid for such a lead time.

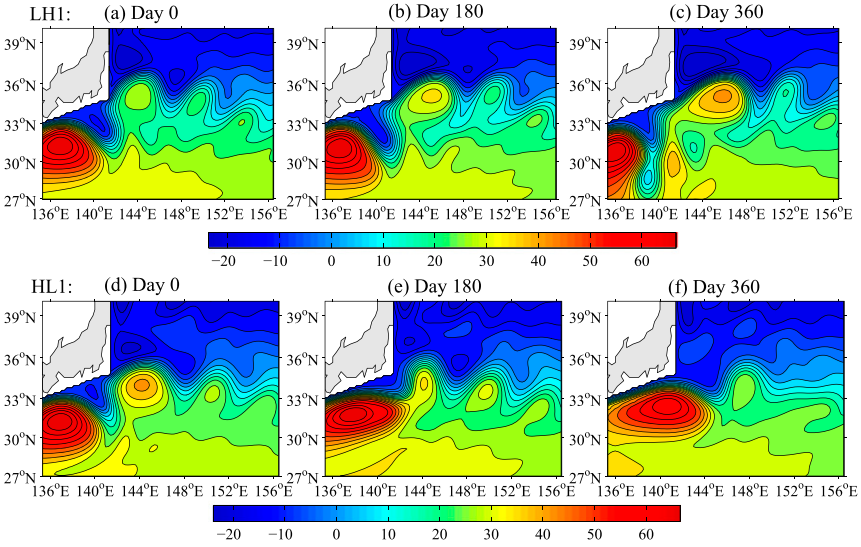

FIG. 4. SSH components (cm) of the KE transition processes (a)–(c) LH1 and (d)–(f) HL1.

For each transition process, we consider that the predictions with the lead time of 180 days are performed starting at every 30 days until the predictions cover the whole transition period of 360 days. Taking LH1 as an example, suppose that its starting time is day 0 (as shown in Fig. 4a); the starting prediction times are day 0, day 30, until day 180, respectively. As such, the seven predictions are performed for each transition process. To investigate the effects of the SV-type initial error on the prediction, the SV is calculated for each prediction. Naturally, the state in the control integration corresponding to each prediction is taken as the background state. Hence, for each transition process we obtain seven background states to compute the SV. These states are labeled in Table 1.

4) Run an ensemble of m forecasts with the lead times of $\Delta t = 180$ days for each background state. In each of the ensemble members, the initial SSH field is perturbed by a random Gaussian white noise with standard deviation 5×10^{-4} m. For each background state, the ensemble mean of the forecasted SSH is denoted by $\overline{\boldsymbol{\psi}_0(t)}$, where $t = t_0 + \Delta t$.
5) Add the leading five EOF modes $\mathbf{e}_i$ ($i = 1, 2, \ldots, 5$) obtained in step 2 to the initial conditions of step 4 to generate five new forecast ensembles (each with m members). To ensure the linearity of the error growth and simultaneously ensure that the resulting prediction errors are not too small, the EOF modes are scaled by a factor of 0.85 (this choice is based on sensitivity experiments). The corresponding ensemble means of the SSH are denoted by $\overline{\boldsymbol{\psi}_i(t)}$.
6) Obtain the reduced-state space matrix $\tilde{\mathbf{L}}$ of the linear propagator $\mathbf{L}$ by minimizing the residual term in the following equations:

$$\mathbf{L}\mathbf{e}_i = \overline{\delta\boldsymbol{\psi}_i(t)} \equiv \overline{\boldsymbol{\psi}_i(t)} - \overline{\boldsymbol{\psi}_0(t)} = \sum_{j=1}^{5} l_{ij}\mathbf{e}_j + \text{residual}, \quad (7)$$

where l_{ij} is the element of the matrix $\tilde{\mathbf{L}}$.

7) Define the initial and final norms to calculate the SV. To measure the amplitude of the initial SSH error, the initial norm is defined as the sum of the squares of the initial errors over the whole model domain; that is, $\|\tilde{\boldsymbol{\eta}}'(t_0)\| = \langle \mathbf{N}\tilde{\boldsymbol{\eta}}'(t_0), \mathbf{N}\tilde{\boldsymbol{\eta}}'(t_0)\rangle$, where the angle

TABLE 1. Details for the chosen KE transition processes that are marked in Fig. 2c. For each transition process, seven background states are determined to compute the SV.

The KE transition phase	Transition process	Starting time (yr)	Transition period (days)	Number of background state
LH phase	LH1	141.918	360	7 (LH1bi, $i = 1, 2, \ldots, 7$)
	LH2	152.690	360	7 (LH2bi, $i = 1, 2, \ldots, 7$)
	LH3	161.480	360	7 (LH3bi, $i = 1, 2, \ldots, 7$)
HL phase	HL1	147.274	360	7 (HL1bi, $i = 1, 2, \ldots, 7$)
	HL2	156.397	360	7 (HL2bi, $i = 1, 2, \ldots, 7$)
	HL3	166.877	360	7 (HL3bi, $i = 1, 2, \ldots, 7$)

bracket represents the inner product, $\tilde{\boldsymbol{\eta}}'(t_0)$ represents the vector that consists of the initial SSH error, and the projection matrix $\mathbf{N}$ equals the identity matrix $\mathbf{I}$. In addition, because the potential energy over the KE region [Eqs. (3)] can well distinguish the different states of the KE, as shown in Fig. 2b, the final norm is defined as the sum of the squares of the SSH predictive error at the final time within the KE region A (Fig. 1); that is, $\|\tilde{\boldsymbol{\eta}}'(t_0+\Delta t)\| = \langle \mathbf{P}\tilde{\boldsymbol{\eta}}'(t_0+\Delta t), \mathbf{P}\tilde{\boldsymbol{\eta}}'(t_0+\Delta t)\rangle$, where $\tilde{\boldsymbol{\eta}}'(t_0+\Delta t)$ represents the vector that consists of the SSH predictive error, and the projection matrix $\mathbf{P}$ is defined to be diagonal with unit entries for the area A and zero elsewhere. Now we have to transform the initial and final projection matrixes in the model space into the reduced-state space, in which the SV is calculated. According to the formulas derived by Tang et al. (2006), the initial and final projection matrixes in the reduced space can be written as follows:

$$\mathbf{N}_R = \mathbf{E}^{\mathrm{T}}\mathbf{N}^{\mathrm{T}}\mathbf{N}\mathbf{E} = \mathbf{I}; \quad \mathbf{P}_R = \mathbf{E}^{\mathrm{T}}\mathbf{P}^{\mathrm{T}}\mathbf{P}\mathbf{E}. \tag{8}$$

In Eq. (8), the columns of $\mathbf{E}$ are the EOF modes $\mathbf{e}_i$. Note that the orthogonality of the EOF modes has been used in Eq. (8).

8) Obtain the SV in the reduced-state space from the following eigenvalue equation:

$$\tilde{\mathbf{L}}^{\mathrm{T}}\mathbf{P}_R\tilde{\mathbf{L}}\mathbf{s}_k = \sigma_k^2\mathbf{s}_k, \tag{9}$$

where $\mathbf{s}_k$ is the kth SV, and σ_k is the kth singular value. The SV $\mathbf{s}_k$ can be transformed back into the model space through $\mathbf{E}\mathbf{s}_k$. Accordingly, the final amplified vector on the model space is $\mathbf{E}(\tilde{\mathbf{L}}\mathbf{s}_k)$.

It can be seen from the above steps that, unlike the traditional procedure for calculating the SV, the ensemble-based strategy does not require the tangent linear and adjoint models. Hence, the strategy is very cost-effective.

3. Singular vector and its robustness

As stated above, the SV can be computed using the ensemble approach. Here the SV is calculated using five EOF modes and 20 ensemble members for each background state (notice that 25 members are used to test the sensitivity for LH1b1 and HL1b1, as shown in section 3b). In this section, we will explore some properties of the SVs for different background states and the sensitivity of the SVs to various choices of the implementation scheme.

a. *The leading SV*

In this study, we consider the leading SV (i.e., the first SV) that has maximum singular value. The average singular value for each transition process is shown in Fig. 5 (see the bars). For each transition process, the maximal and minimal singular values obtained from seven different background states are also plotted in the figure, as indicated by the top and bottom error bars. Interestingly, although the singular values for different background states are different, the average singular values for the HL transition phases are larger than those for the LH phases. The minimal singular value for the HL phase is also larger than the average value for the LH phase. These indicate that the SVs generally grow faster in the HL phases than in the LH phases. That is to say, the growing rates of the SVs depend on the transition phases of the KE. From the point of view of the error growth, the transition processes belonging to the LH phase appear to be more predictable than those of the HL phase, because the initial errors grow more slowly in the LH phase. This is consistent with the result derived from the Lyapunov exponents computed by Pierini et al. (2009).

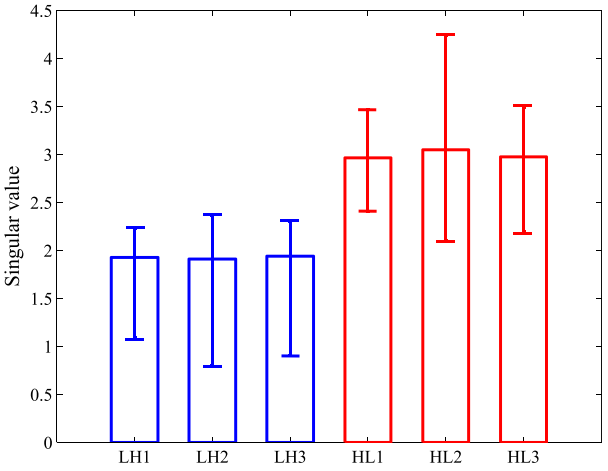

FIG. 5. Mean of singular values for seven background states in each transition process. Blue and red bars denote the mean values for the LH phase and the HL phase, respectively. The maximal and minimal singular values for each transition process are represented as error bars.

Figure 5 indicates that the average singular values are close for the same transition phase of the KE. Furthermore, the singular values for the first background states in the transition processes LH1 and HL1 (denoted by LH1b1 and HL1b1; their patterns are shown in Figs. 4a,b and 4d,e) are 2.0 and 3.0, respectively, which is very close to the mean singular values for the LH and HL phases. For simplicity, we choose LH1b1 and HL1b1 to present the results in the following analysis.

The spatial patterns of the SVs for LH1b1 and HL1b1 are shown in Fig. 6 (shaded). It is found that although the specific patterns for different background states are different, both SVs have large negative

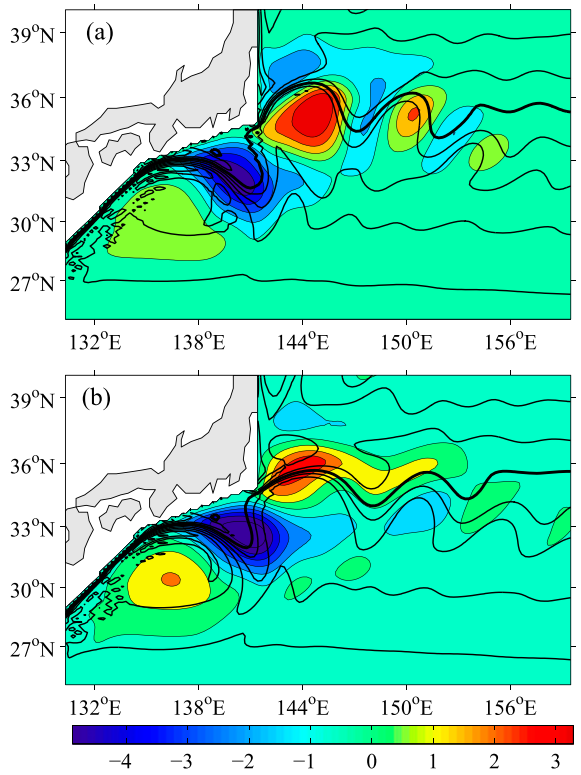

FIG. 6. The first SV modes for SSH anomalies (shaded; cm) and the PV distributions of the initial background states (contours, interval = $1.3 \times 10^{-8}\,s^{-1}\,m^{-1}$) for (a) LH1b1 and (b) HL1b1. The thick contour line denotes the $1.68 \times 10^{-7}\,s^{-1}\,m^{-1}$ PV level.

anomalies in the KLM region south of Japan [around (32°N, 139.5°E)] and positive anomalies in the first crest region of the KE [around (35°N, 144°E)]. To further investigate the pattern features of the SVs, the potential vorticity (PV) distributions of the initial background states are also plotted in Fig. 6 (contour). It is found that the large values of the SV-type initial errors almost lie in the PV frontal region and its adjacent area, especially in the KLM region. As pointed out by Kramer et al. (2012), these are areas where barotropic instability may take place. Hence, the errors in these regions can grow faster. The concrete mechanism of the error growth will be analyzed in section 4b.

The above discussion has illustrated the essential features of the singular values and SVs for different background states. In section 4, we will investigate the evolution processes of the SV and its growing mechanism. Before that, however, the robustness of the SV must first be assessed.

b. *Robustness of the leading SV*

We first examine the convergence of the leading SV with respect to the number of the EOFs. Figure 7 shows the patterns of the leading SVs with different numbers of EOFs for LH1b1 and HL1b1, with a fixed ensemble size $m = 20$. The convergence of the SV pattern can be visually estimated from the figure. More specifically, the dominant patterns are well represented by using three to five EOFs for both LH1b1 and HL1b1. In addition, a similar convergence can also be seen from the patterns of the corresponding final amplified vector (not shown). This implies that computing the leading SV based on the leading five EOFs is appropriate, as done in this study.

In addition, the SV also depends on the choice of the number of ensemble members. To examine this dependence, we calculate the SV using different numbers of ensemble members with five fixed EOFs. The obtained singular values for a different number of ensemble members are plotted in Fig. 8. For both LH1b1 and HL1b1, the singular values converge to the individual steady values when more than ~15 ensemble members are used. We also investigate the changes of the patterns of the SVs for LH1b1 and HL1b1 as the number of ensemble members increases: the patterns are very similar for different numbers of ensemble members (not shown). Thus, the estimated SV and singular value are reliable when using more than 15 ensemble members. In this study, we use 20 ensemble members to compute the SV.

As discussed in section 2, the SV is obtained from the tangent linear approximation of the nonlinear model, which assumes that the growth of the error in the nonlinear model can be approximated by its linear growth. To examine the validity of the linear approximation, we superimpose the SVs shown in Fig. 6 (scaled by the factor 0.85) on the corresponding initial background state at time t_0 and then integrate the nonlinear model for $\Delta t =$ 180 days. The difference between the integration result and the background state at time $t_0 + \Delta t$ represents the nonlinear growth of the SV. Figure 9 compares the nonlinear growth of the SV and its final amplified vector from the linear propagator for LH1b1 and HL1b1. The figure demonstrates that although there are some small differences between the nonlinear growth of the SV and the final amplified vector, the main features of the patterns are very similar. For example, the significant negative anomalies in the KLM region and the positive anomalies in the first crest region of the KE can be clearly seen for both the nonlinear growth and the final amplified vector. This reveals that the linear approximation is valid and the calculations of the SVs are robust.

4. Growth of the SV and its mechanism

a. *Growth process of the SV*

The analysis of section 3a has revealed the basic properties of the SVs and singular values. In this

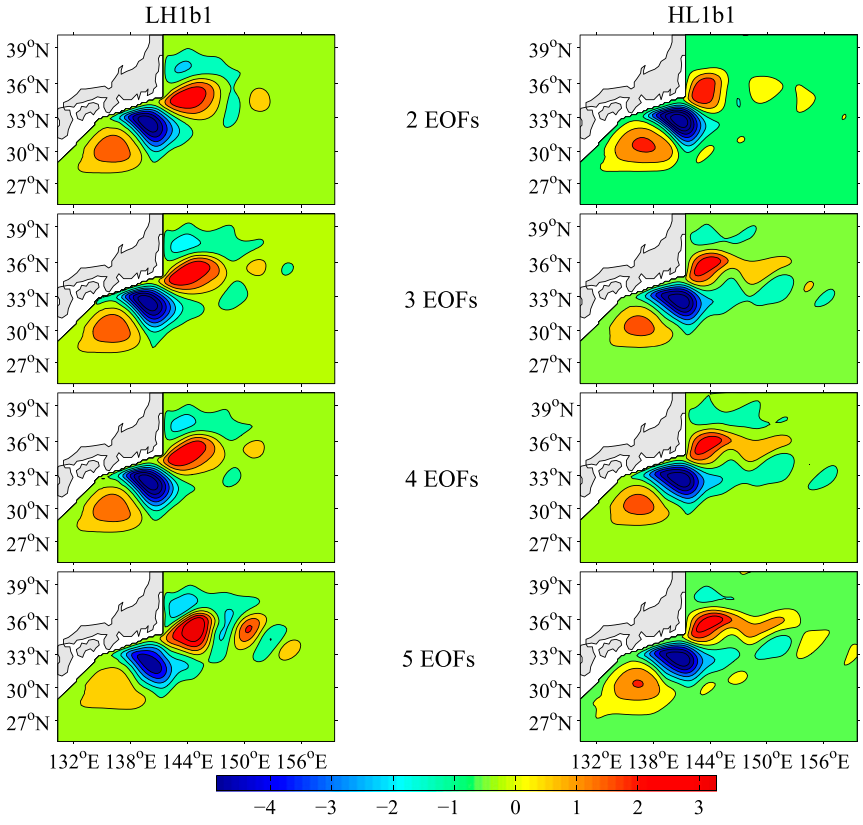

FIG. 7. The first SVs of SSH anomalies (cm) obtained by using different numbers of EOFs for the background state (left) LH1b1 and (right) HL1b1.

subsection we investigate the growth processes of the SVs and their effects on the short-range prediction of the KE state. It is worth mentioning that the sign of the SV is arbitrary because of the linear assumption. So we will explore the growth processes for both the positive and negative SVs (denoted by +SV and −SV) in the nonlinear model.

To investigate the growth processes of the +SV and −SV, we carried out two model integrations. In these two integrations, the +SV and −SV (scaled by the factor 0.85) are respectively superimposed on the initial background state. The differences between the integration results and the background state at the corresponding time reflect the growth processes of the +SV and −SV: these are shown in Figs. 10 and 11 for the SSH anomaly components for LH1b1 and HL1b1. We can see from the figures that the errors evolve gradually as time increases and the growth processes are similar for +SV and −SV but with opposite sign, especially for LH1b1.

More specifically, for LH1b1, the evolution of the +SV (Fig. 10, left) indicates that both the positive anomalies located over the first crest of the KE and the negative anomalies in the KLM region strengthen. This may result in the intensification of the first crest (anticyclonic meander) of the KE and the cyclonic meander in the KLM region. To confirm this, we examine the SSH patterns from the integrations obtained with superimposing the +SV and −SV onto the initial background states, for LH1b1 and HL1b1, respectively, as shown in Fig. 12. Figure 12a indicates that the first crest of the KE and cyclonic meander south

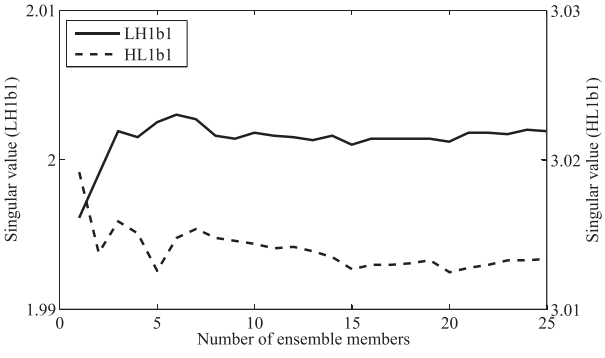

FIG. 8. The evolution of the first singular values with the number of ensemble members for the background states LH1b1 (solid line left *y* axis) and HL1b1 (dashed line right *y* axis).

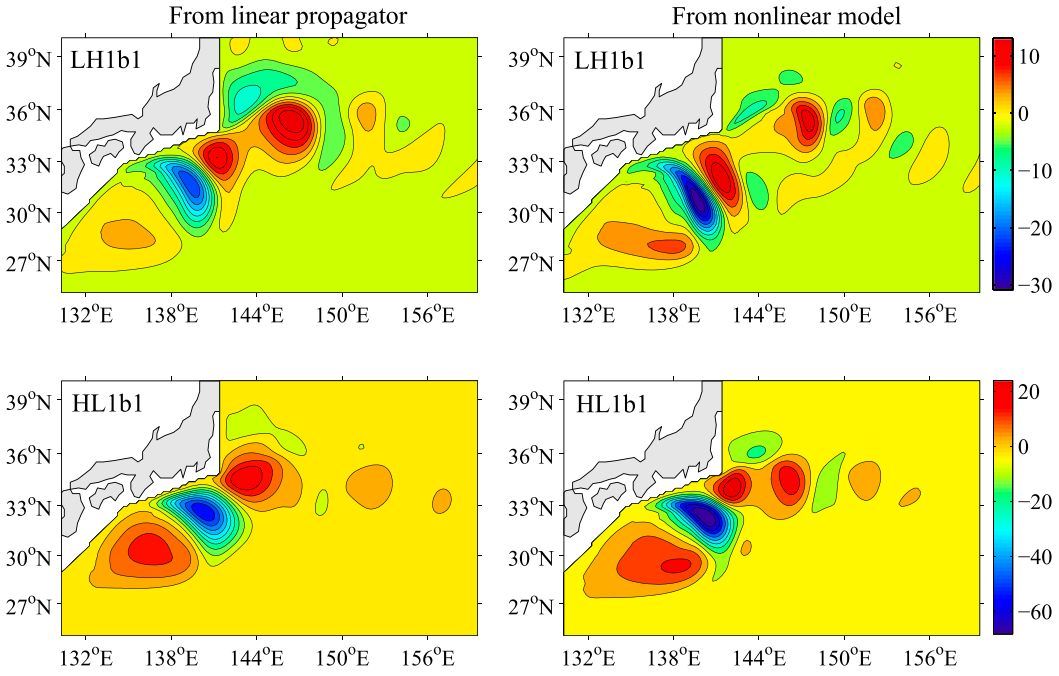

FIG. 9. SSH anomaly components (cm) of the final amplified vector from (left) the linear propagator and (right) the final state of the nonlinear growth of the SVs derived from the nonlinear model at time $t_0 + \Delta t$ for the background states (top) LH1b1 and (bottom) HL1b1.

of Japan are indeed stronger than the background state shown in Fig. 4b. The enhancement of the first crest further induces the KE to strengthen and to transit toward the high-energy state. Considering that the background state LH1b1 represents the transition process of the KE from the low-energy to the high-energy state, the +SV error promotes the forecasted KE to evolve toward the high-energy state more quickly.

An almost opposite growth process for the −SV can be seen from Fig. 10 (right column). The intensifications of the negative anomalies located over the first crest of the KE and the positive anomalies in the KLM region reduce the strength of the first crest and the cyclonic meander south of Japan (cf. Figs. 12b and 4b), which prevents the KE from shifting toward the high-energy state, leaving it in the low-energy state (Fig. 12b).

For HL1b1, the evolution processes of the +SV and −SV are broadly similar to those for LH1b1, but the transition process in the background state is opposite to that of LH1b1. Hence, the +SV error suppresses the shift of the KE from the high-energy to the low-energy state so that the forecasted KE remains in the high-energy state (Fig. 12c). On the contrary, the −SV enhances the transition process so that the forecasted KE weakens. As shown in Fig. 12d, the first crest of the forecasted KE can hardly be identified.

We have also analyzed the growth processes of the SVs for other background states listed in Table 1. It is found that although the details in the error growth processes can slightly change for the same transition phase, the main features are similar. For the LH phase, the +SV errors cause the forecasted KE to transit from the low-energy to the high-energy state more quickly, while the −SV errors can suppress this transition process. The opposite situation is found for the HL phase. Furthermore, for most of the background states (17/21) in the HL phase, the SV errors grow more quickly than in the LH phase. This is consistent with the results obtained by comparing the singular values, as illustrated in section 3a.

In summary, the evolution of the SV type initial errors has important impacts on the short-range prediction of the transition processes of the KE bimodality. The initial error with the +SV pattern (the positive anomalies located over the first crest of the KE and the negative anomalies in the KLM region) tends to strengthen the KE and shift the KE toward the high-energy state, while the error with the −SV pattern tends to weaken the KE and lead to the low-energy state. Also, the error growth depends on the transition phases of the KE bimodality.

b. Analysis of the error growth mechanism

In this subsection, we will explore the dominant mechanism causing the SV growth. Two questions will be addressed: (i) What physical processes are responsible for the fast growth of the SV? (ii) Are the

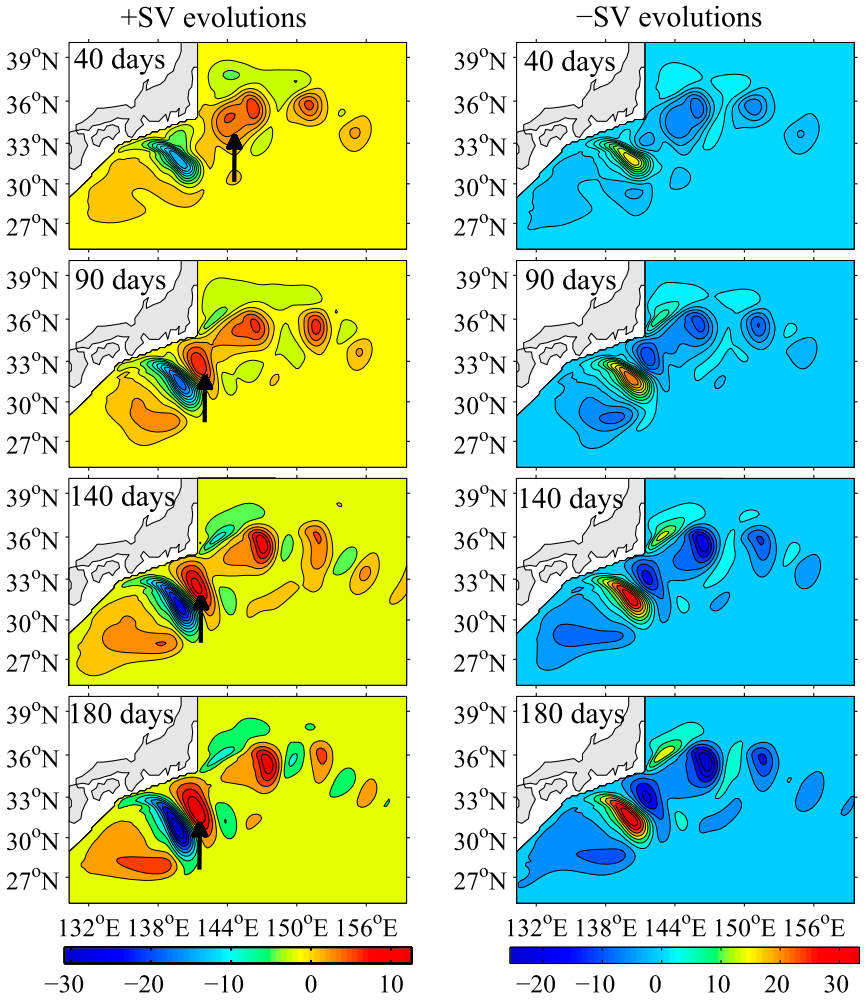

FIG. 10. SSH anomaly components (cm) of the nonlinear evolution processes of the (left) +SV and (right) −SV for the background state LH1b1.

mechanisms of the error growth different for the HL phase and the LH phase?

To reveal the mechanism of the error growth, a perturbation energy analysis is performed. Here we examine the changes of the perturbation kinetic energies in the growth processes of the SVs. The perturbation kinetic energy is defined as follows:

$$E'_K(t) = \frac{1}{2}\iint_A (h_b + \eta')[(u')^2 + (v')^2]\,dx\,dy, \quad (10)$$

where $h_b = D + \eta_b$ is the upper-layer thickness component of the background state and η', u', and v' denote the perturbations of the corresponding model variables resulting from the growths of the SV initial errors. Because we mainly focus on the error growth in the KE region, the integration domain A in Eq. (10) is chosen as the KE region shown in Fig. 1.

We display the time series of the perturbation kinetic energies caused by +SV and −SV for LH1b1 and HL1b1 in Fig. 13. Obviously, the perturbation kinetic energies for both LH1b1 and HL1b1 show the increasing trend. Also, the perturbation kinetic energies are larger for HL1b1 than for LH1b1 at day 180. This implies that the errors for HL1b1 acquire more energy in their growth processes.

To further investigate what physical process causes the increase of the perturbation kinetic energy, we derive the evolution equation of the perturbation kinetic energy based on the model Eq. (1), which is shown in the appendix. For convenience, we denote the perturbation kinetic energy at each model grid as follows:

$$E'_{K,g}(t) = \frac{1}{2}(h_b + \eta')[(u')^2 + (v')^2]. \quad (11)$$

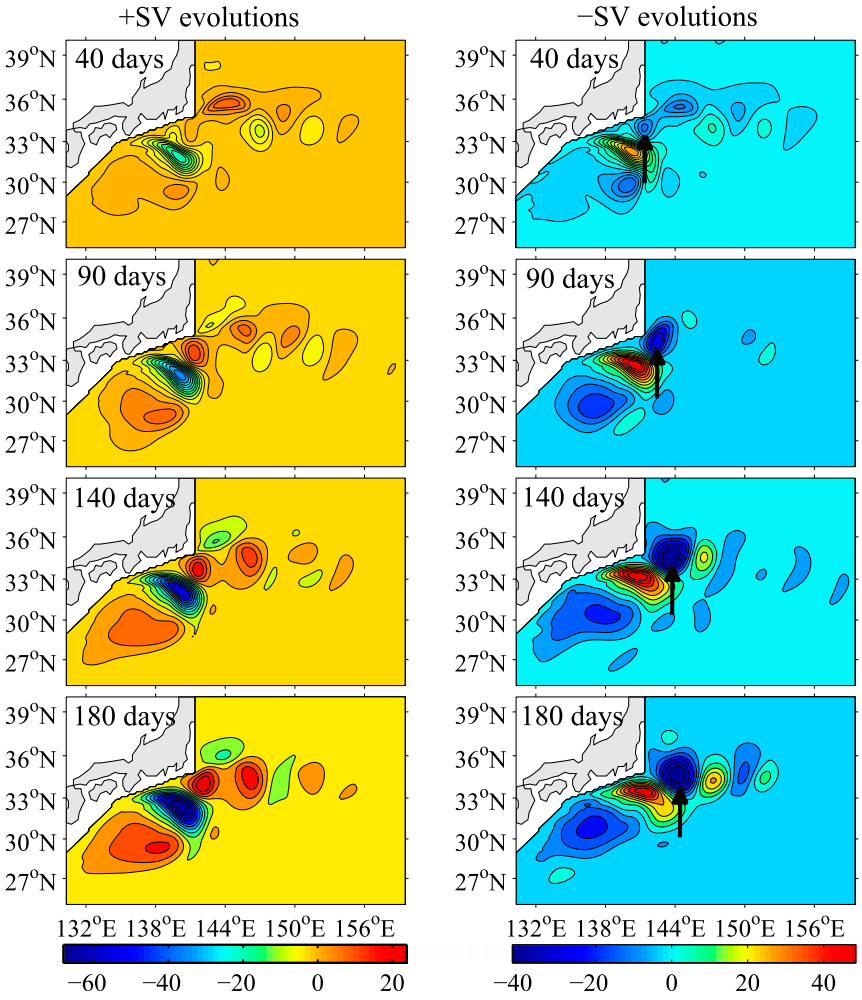

FIG. 11. As in Fig. 10, but for the background state HL1b1.

As shown in the appendix, the evolution of the perturbation kinetic energy can be formally written as

$$\frac{\partial E'_{K,g}(t)}{\partial t} = \mathrm{ADV} + \mathrm{BT} + \mathrm{DIV} + \mathrm{VF} + \mathrm{WIND}, \qquad (12)$$

where the first term on the right-hand side denotes the advection (ADV) effect caused by the SV perturbation, the second term is the barotropic (BT) conversion rate from background kinetic energy to perturbation kinetic energy caused by barotropic instability, the third term represents the evolution of perturbation kinetic energy induced by the velocity divergence (DIV) of perturbation field, the fourth term is the contribution of the lateral eddy viscosity and the interfacial friction (VF), and, finally, the fifth term denotes the contribution of the wind stress (WIND). The expressions of these terms are listed in the appendix.

To quantify the contribution of each term, we integrate them over the KE region A (Fig. 1). The results are shown in Fig. 14. Interestingly, the figure indicates that the dominant positive contribution to the evolution of the perturbation kinetic energy in the KE region is the BT term for LH1b1 and the ADV term for HL1b1, while the dominant negative contributions are provided by the ADV and VF terms. The same analysis has also been performed for other background states. Similar results are obtained: the BT term plays a dominant role in the growth of the SV errors within the KE region for the LH phase, while for the HL phase the dominant role is the ADV term. On the other hand, the ADV and VF terms play the opposite roles in the error growth, respectively.

To explore why the dominant physical processes that are responsible for the error growth in the KE region are different for different transition phases, we first investigate the horizontal velocity shear in the background states because this is related to the BT term [see Eq. (A9)]. The spatial distribution of the magnitude of the flow velocity shear, that is

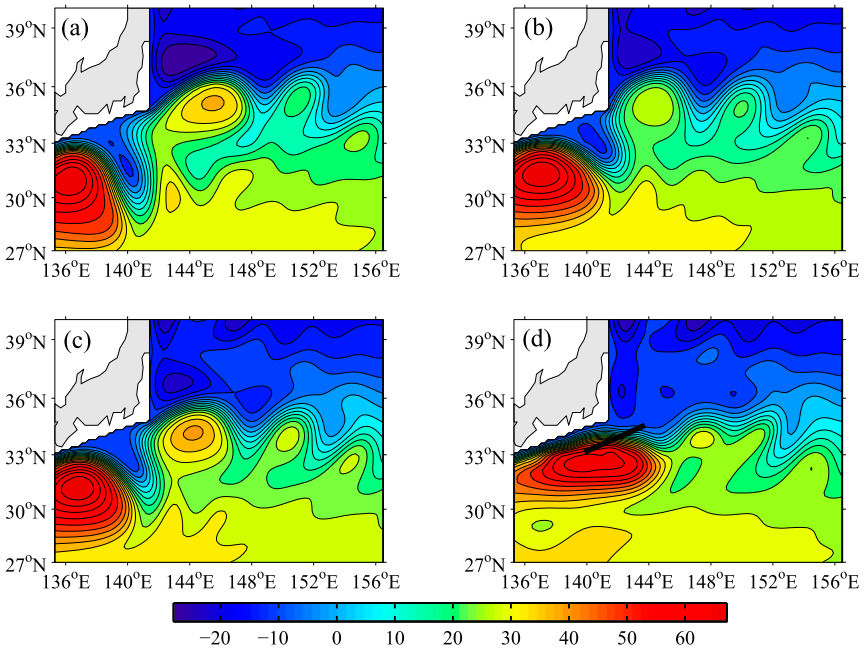

FIG. 12. SSH patterns (cm) of the integrations of the nonlinear model from superimposing the (a),(c) +SV and (b),(d) −SV on the initial background states for (top) LH1b1 and (bottom) HL1b1. The black solid line in (d) is used to plot the Hovmöller diagrams of SSH in Fig. 18.

$$\sqrt{(\partial u_b/\partial x)^2 + (\partial u_b/\partial y)^2 + (\partial v_b/\partial x)^2 + (\partial v_b/\partial y)^2}$$

is shown in Fig. 15. It can be seen that the shear in the KLM region is strong for both LH1b1 and HL1b1, while it is stronger in the KE region for LH1b1 than for HL1b1, especially after 90 days: this may be induced by the position of the Kuroshio at the southeastern edge of Japan in the background states. Figure 4 indicates that the position of the Kuroshio in the background state LH1b1 is closer to the southeastern edge of Japan [at about (35°N, 141°E)] than that in the HL1b1. Because of the eddy viscosity, a stronger velocity shear is formed in the KE region for LH1b1. This can explain why the barotropic energy conversion associated with the velocity shear plays a dominant role in the error growth within the KE region for LH1b1.

As shown in Eq. (A9), the barotropic energy conversion is also related to the error distribution. Only when the error structure matches the horizontal velocity shear, the barotropic energy conversion (BT term) is significant. Hence, to check the barotropic energy conversion, the distribution of the BT term should be analyzed. For simplicity, we only consider the BT terms during the +SV evolution for LH1b1 and the −SV evolution for HL1b1. These two cases are chosen because they exhibit the KE transition process between the low- and high-energy states, so they can shed light on the KE transition mechanism. However, for −SV (+SV) evolution in LH1b1 (HL1b1), the initial KE takes the low (high) energy state and the final KE is still in the low (high) energy state, as shown in Fig. 12b (Fig. 12c). Of course, regardless of the +SV and −SV evolutions, the qualitative results obtained for the BT term in the same background state are basically similar because the velocity shear is the same (Fig. 15). Figure 16 indicates the distribution of the BT terms. For both LH1b1 and HL1b1, the BT terms in the KLM region are positive and large, indicating that the error growth in the KLM region is mainly due to the barotropic energy conversion

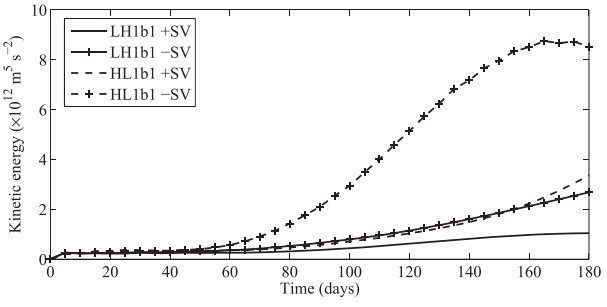

FIG. 13. Time series of the perturbation kinetic energy corresponding to the growths of the +SV (lines without symbols) and −SV (lines with symbols) for LH1b1 (solid line) and HL1b1 (dashed line). The kinetic energy is calculated using Eq. (10).

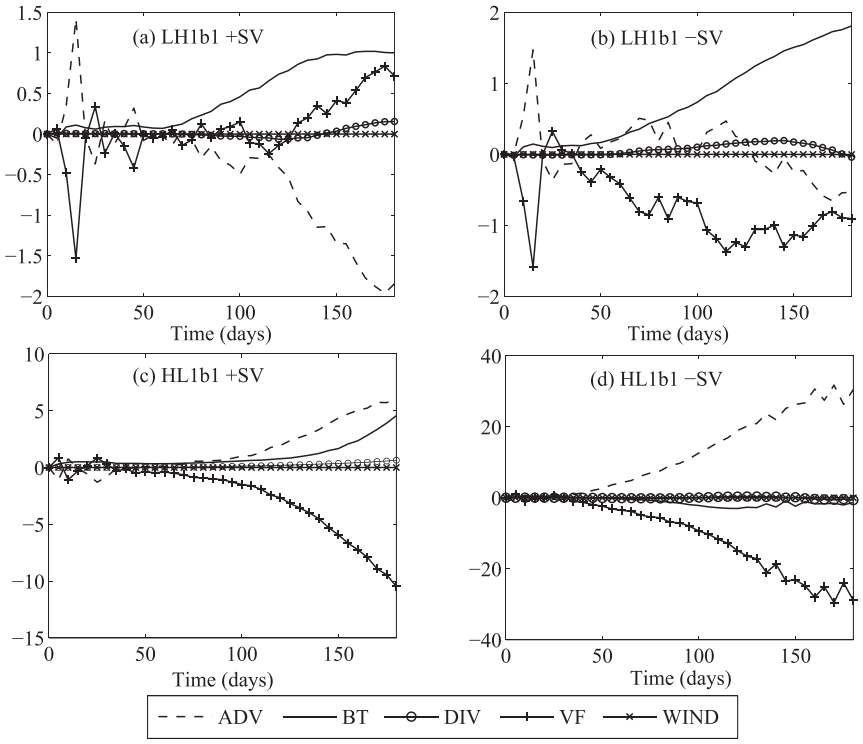

FIG. 14. Contribution of each term in Eq. (12) integrated over the KE region A (Fig. 1) to the evolution of the perturbation kinetic energy (10^6 m^5 s^{-3}) induced by the (a),(c) +SV and (b),(d) −SV for the (top) LH1b1 and (bottom) HL1b1.

associated with the barotropic instability. However, for the KE region, the situations are different: the values of the BT term are positive in the KE region for LH1b1, while they are basically negative for HL1b1, which is consistent with Figs. 14a and 14d. This implies that the barotropic energy conversion can cause fast growth of the SV error in the KE region for LH1b1 but not for HL1b1.

It is worth noting that the ADV term acts against the BT term for the +SV evolution in LH1b1 (Fig. 14a). The spatial distribution of the ADV term shown in Fig. 17a indicates that a weak positive ADV distribution exists around (31°N, 140.5°E) and a negative distribution exists to the eastern side after 90 days, which seems to correspond to the advection of the positive SSH anomaly from the KE region to the KLM region shown in the left column of Fig. 10 (see the arrows). This causes the decrease of the perturbation kinetic energy in the KE region.

In the following, we examine the role of the advection process in the error growth for –SV evolution in HL1b1. Figure 17b shows the distribution of the ADV term, which indicates that the ADV term exhibits the large positive values in the KE region, implying that the advection process plays an important role in the error growth in the KE region. In addition, we also examine the distribution of the VF term acting against the ADV term. It is similar to that of the ADV term but with opposite sign (figure not shown). This evidences that part of the perturbation kinetic energy induced by the advection effect is dissipated by the eddy viscosity and interfacial friction and the remaining part contributes to the growth of the perturbation.

As discussed above, the evolution of the perturbation kinetic energy in the KE region is mainly caused by the barotropic instability for LH1b1 and the advection process for HL1b1, respectively. Hence, we can now explain the evolution process of the perturbation and the strengthening and weakening of the KE thus induced. For the +SV evolution in LH1b1, the initial +SV structure consists primarily of a negative SSH anomaly in the KLM region and a positive anomaly in the KE region. Because of barotropic instability related to the horizontal velocity shear in the background states, these two anomalies can achieve continuous growth, which produces the growth process of the SSH anomalies evidenced in Fig. 10 (left column). The evolution of the positive SSH anomaly in the KE region results in the KE strengthening. For the −SV evolution in LH1b1

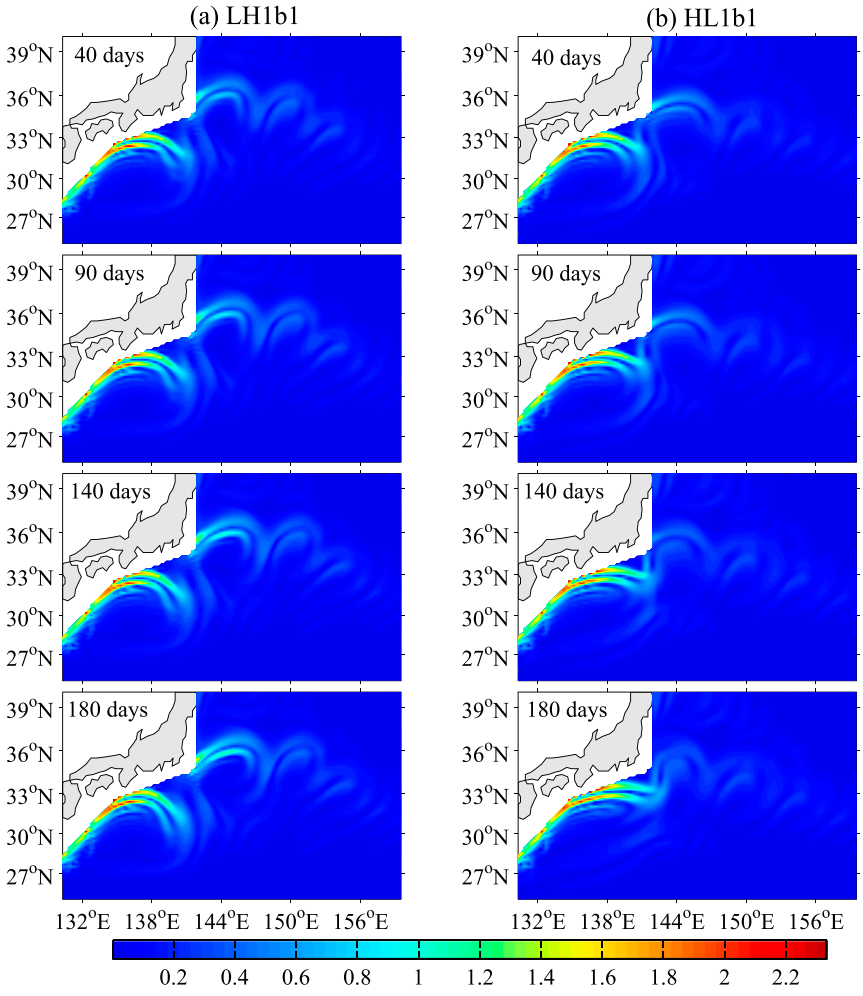

FIG. 15. Horizontal velocity shear ($10^{-5}\,s^{-1}$) in the background state (a) LH1b1 and (b) HL1b1.

(Fig. 10, right), the pattern of the initial SSH anomaly is opposite to that of the +SV. In this situation, the evolution process of the SSH anomalies caused by −SV is almost opposite to that induced by +SV, which leads to the weakening of the KE.

For HL1b1, different physical processes are responsible for the growth of the perturbation kinetic energy in the KLM and KE regions. Barotropic instability and advection processes play dominant roles in the growth of the perturbation kinetic energy in the KLM and KE regions, respectively. The barotropic instability leads to the growth of the perturbation kinetic energy in the KLM region. Then, the growing perturbation is advected toward the KE region, which can be recognized in Fig. 11, especially in the right column (see the arrows). More specifically, for the +SV evolution in HL1b1 (Fig. 11, left), one should consider that during the weakening process of the KE, the Kuroshio meander acts as a barrier; in other terms, when the Kuroshio meander is strong, the cyclonic eddy is constricted between the main axis of the Kuroshio meander and the southern coast of Japan (e.g., see Fig. 4d), so that the positive vorticity advection toward the KE region is hindered. The positive SSH anomaly in the KE region in the +SV suppresses the weakening of the KE. Simultaneously, the negative SSH anomaly in the KLM region, which grows rapidly due to barotropic instability, induces the increase in the amplitude of the Kuroshio meander south of Japan. Hence, the barrier role of the Kuroshio meander will strengthen. In this situation, the negative SSH advection toward the KE region in the background state will weaken.

To further analyze the advection effect, we investigate the variations of the SSH field obtained after superimposing the SV errors. The results are presented in

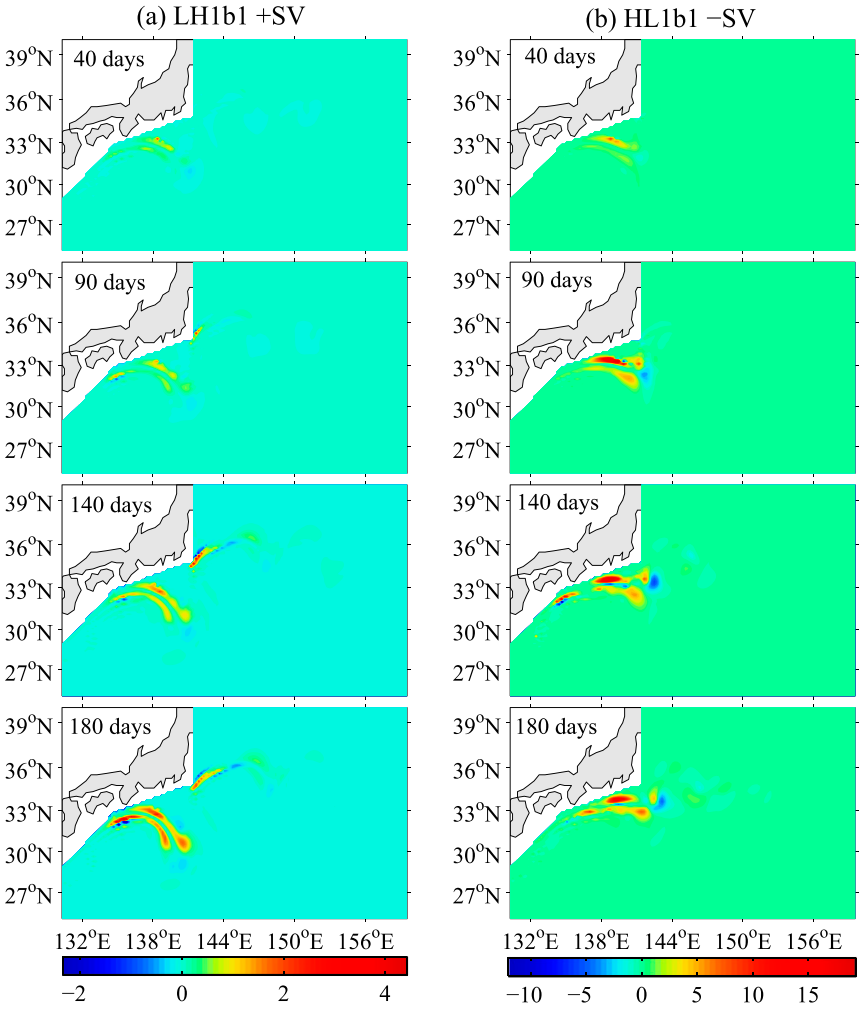

FIG. 16. Spatial distribution of the BT term (10^{-4} m^3 s^{-3}) in Eq. (12) for (a) the +SV evolution in the LH1b1 and (b) the −SV evolution in the HL1b1.

Fig. 18, in which the Hovmöller diagrams of the SSH along the transect in Fig. 12d are reported. Figure 18a shows that a weak advection of the negative SSH from the KLM to the KE region occurs after 140 days in the background state, while the advection process in the +SV error evolution can hardly be seen (Fig. 18b). This provides a further confirmation that the advection effect induced by the +SV error tends to suppress the advection of the negative SSH in the background state, which thus increases the positive SSH anomaly in the KE region and causes the KE to be stronger than that in the background state.

By contrast, for the −SV evolution in HL1b1 (Fig. 11, right), the −SV error structure tends to weaken the barrier role, which tends to strengthen the advection of the negative SSH. Indeed, Figs. 18a and 18c clearly indicate that the advection is strengthened after superimposing the −SV error. As such, the SSH over the KE region in the background state is reduced, which thus intensifies the negative SSH anomaly and contributes to the weakening of the KE.

The above analysis reveals that different physical processes are responsible for the error growths in the KE region for different KE transition phases. By comparing the top and bottom lines in Fig. 14, the values of the BT term for LH1b1 are found to be much smaller than those of the ADV term for HL1b1 (note that the ordinate scale is different in the figures). This may explain why the error in the KE region grows faster in the HL phase.

c. *Connection between the KLM and the KE*

The above analysis shows that the evolution of the SSH anomaly in the KE region is related to that in the

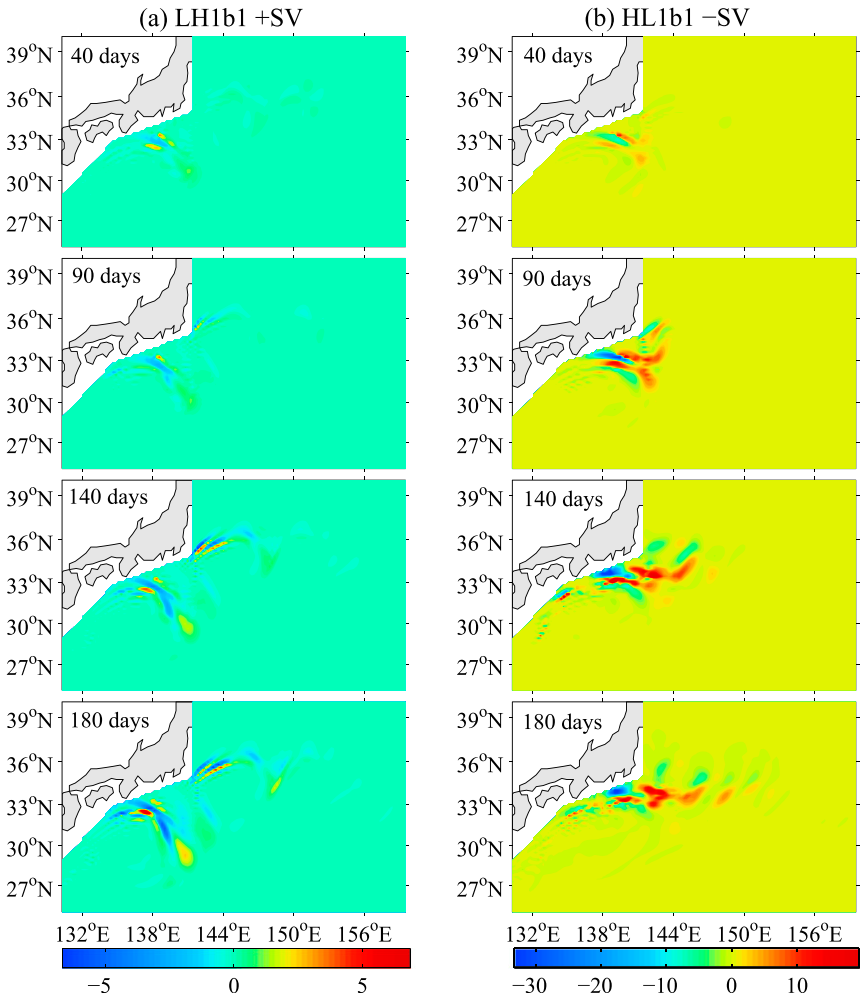

FIG. 17. As in Fig. 16, but for the ADV term.

KLM region. This implies that the KLM variation may have an effect on the change in the KE states. To reveal such effects, this subsection will investigate the KE transition processes promoted by the +SV evolution in the LH1b1 and the −SV evolution in the HL1b1.

The following numerical experiments are performed: we first remove the SSH anomalies in the KLM region (28°–35°N, 136°–140°E) from the initial SV errors and then integrate the numerical model and compare the results with those obtained without removing the anomalies. For the +SV in LH1b1, only the negative SSH anomaly in the KLM region is removed. This results in smaller prediction error in the KE region (cf. Figs. 19a and 19b), although the difference is less than 5 cm, which reflects that the negative SSH anomaly in the KLM region plays a role in promoting the positive SSH anomaly growth in the KE region. The reason may be that the existence of the negative SSH anomaly in the KLM region produces a strong pressure gradient, which, in turn, induces a northern flow velocity anomaly on the right-hand side of the KLM. Such an anomaly will strengthen the northern Kuroshio velocity around 140°E. So the KE will be intensified and simultaneously the horizontal velocity shear in the KE region may also strengthen: this can enhance the evolution of the positive SSH anomaly in the KE region. As we know, a negative SSH anomaly in the KLM region corresponds to the increase in the magnitude of the KLM. Hence, the strengthening of the KLM may be able to promote the KE to shift from the low- to the high-energy state.

On the contrary, for the −SV in HL1b1, only the positive SSH anomaly in the KLM region is removed. The results show that it has very significant effects on the error growth in the KE region (cf. Figs. 19c and 19d),

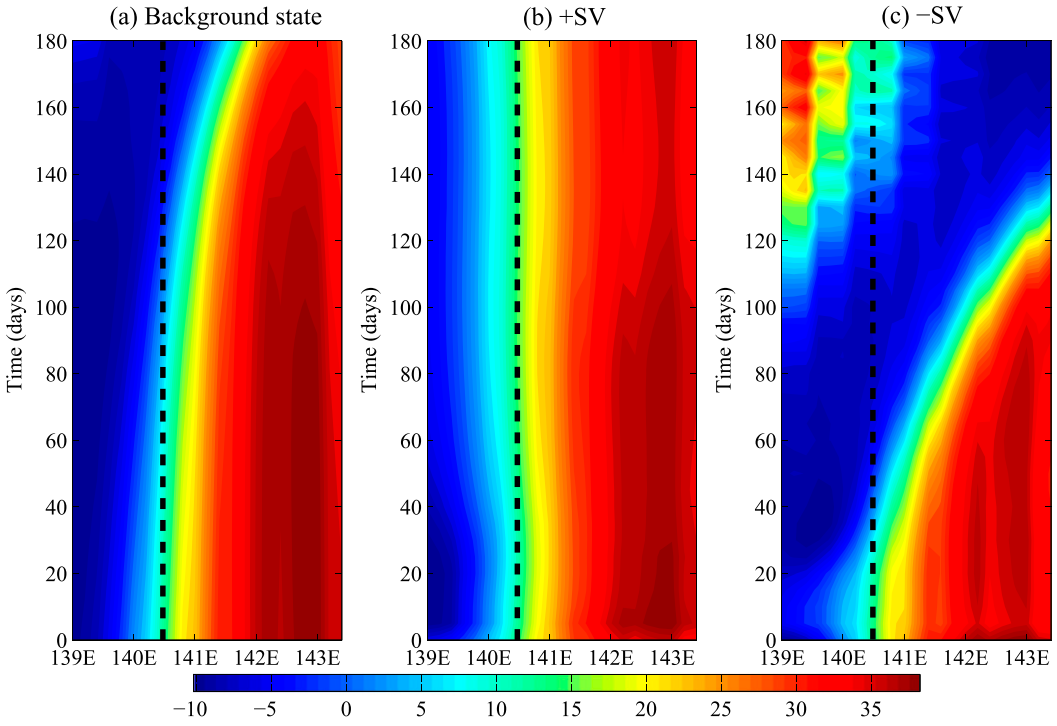

FIG. 18. Hovmöller diagrams of SSH (cm) for (a) the background state HL1b1 and obtained after superimposing (b) +SV and (c) −SV along the transect in Fig. 12d. The dashed line marks the separation between the KLM and the KE regions.

implying that the error evolution in the KE region is mainly caused by the growth of the positive SSH anomaly in the KLM region. This is because the latter evolution reduces the strength of the Kuroshio meander, which will in turn weaken the barrier role of the Kuroshio meander and strengthen the advection of the negative SSH in the KLM region toward the KE region (see the previous subsection). Eventually, the KE will weaken remarkably. So the weakening of the Kuroshio meander will enhance the KE transition from the high- to the low-energy state.

5. Conclusions

We have investigated the effects of the optimal initial error on the short-range prediction of transition processes of the KE bimodality through the SV approach using a reduced-gravity shallow-water ocean model. Based on two almost opposite transition phases of the KE, the SV-type optimal initial errors are calculated using an adjoint-free ensemble-based strategy. The robustness of the SV has been examined through sensitivity experiments. The spatial structures, growth processes, and impacts of the SVs have been analyzed in detail.

Our results show that the large values of the SVs are mainly located in the first crest region of the KE and in the KLM region south of Japan. Also, the SVs can achieve fast growth and have important impacts on the short-range prediction of transition processes between the KE bimodalities. More specifically, although the dynamic mechanisms of the error growths in the KE region are different for different KE transition phases, their effects on the KE prediction are similar: the initial error with +SV pattern (with positive anomalies in the first crest region of the KE and negative anomalies in the KLM region) tends to strengthen the KE and shift the KE path toward the high-energy state, while the initial error with −SV pattern (which is opposite with +SV pattern) is prone to weaken the KE and shift the KE path toward the low-energy state. In addition, the growth rates of the SVs depend on the transition phases of the KE. In the HL transition phase, the SVs grow more quickly than those in the opposite transition phase, implying that the predictability of the transition process in the HL phase is lower than that in the LH phase. The perturbation energy analysis indicates that the dominant physical processes responsible for the error growths in the KE region are different for different transition phases of the KE. In the LH phase,

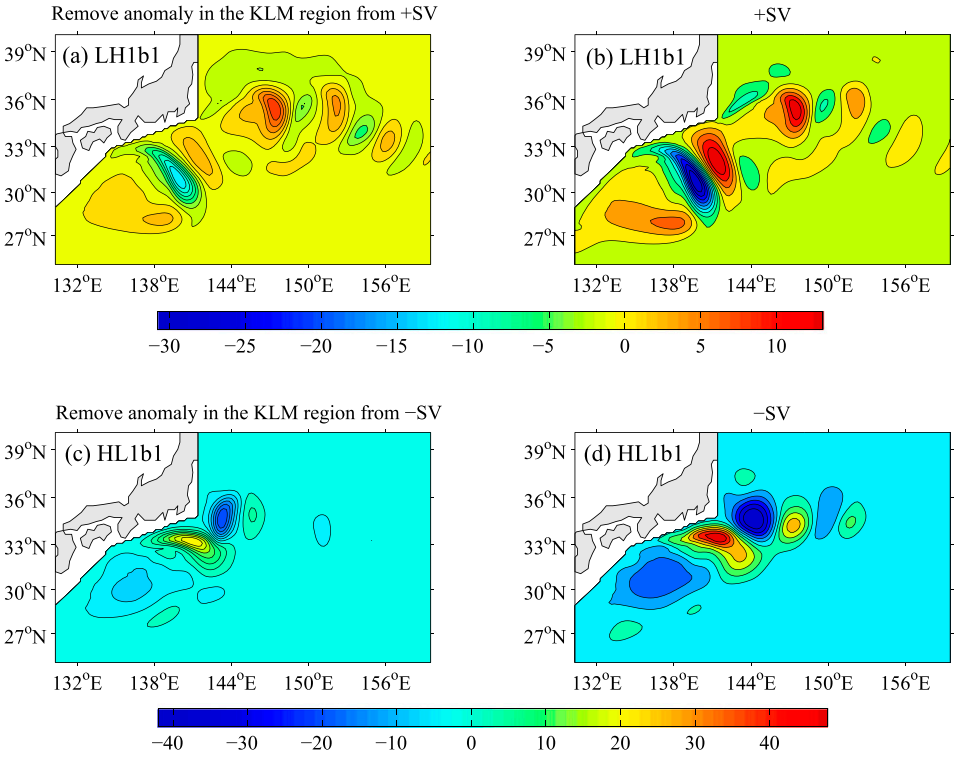

FIG. 19. Distribution of the SSH prediction error (cm) at day 180 caused by (b),(d) the SV error and (a),(c) the error obtained through removing the SSH anomaly in the KLM region from the initial SV error for (top) the +SV evolution in the LH1b1 and (bottom) the −SV evolution in the HL1b1.

barotropic instability plays a dominant role in the error growths, while in the opposite phase the error evolution in the KE region is mainly caused by advection processes.

Furthermore, the SV analysis also reveals the possible connection between the KLM and the KE. The strengthening of the KLM tends to promote the KE to shift from the low- to the high-energy state, while the weakening of the Kuroshio meander is prone to enhance the opposite transition. Interestingly, studies based on observational data (e.g., Sugimoto and Hanawa 2012; Seo et al. 2014) also revealed that the changes in the KE and those in the Kuroshio south of Japan are interrelated. Of course, we should note that this study mainly focus on the short-range prediction of the KE transition. So the discussion about the relationship between the Kuroshio meander south of Japan and the KE state is based on the short time scale. For the decadal time scale, the connection between them needs to be further analyzed.

This study has shed light on the important link between the SV error growth and the intrinsic oscillation of the KE bimodality. As discussed in section 4b, the oceanic intrinsic process causes the SV errors to grow rapidly; the growing errors change the strength of the first crest of the KE and the Kuroshio meander south of Japan (Figs. 10–12), which plays a key role in sustaining the intrinsic oscillation of the KE bimodality as Pierini (2006) pointed out, and therefore enhance or suppress the intrinsic shifting process between the KE bimodalities. This indicates that the initial error growth has significant effects on the short-range prediction of the KE transition process. Hence, the correlation analysis between the wind field and the KE [e.g., as done by Nonaka et al. (2012) and Qiu et al. (2014)] may not be sufficient to predict the variations of the KE system. It is therefore suggested that both the error growth and the correlation between atmosphere and the KE should be considered to predict future variations of the KE state.

The current study has demonstrated some features of the optimal initial errors, including the spatial patterns and growing processes, using the SV method. These results could allow us to effectively generate initial perturbations for the development of an ensemble prediction system of the KE. In addition, the patterns

of the SVs exhibit interesting spatial characteristics: they yield large values over the first crest of the KE and in the KLM region south of Japan. This means that that intensive observations carried out in these areas may reduce the initial error and improve the forecast skill of the transition processes of the KE. In fact, by using a particle filter method, Kramer et al. (2012) also found that these two regions are important for improving the prediction of the KE system. However, Kramer et al. (2012) mainly focused on the long-range (more than 2 years) prediction of the KE, while our SV analysis can significantly contribute to designing an observation system for the short-range prediction of the KE.

The model used in this study is relatively simple compared to OGCMs; nonetheless, it was shown to provide a mean jet and KE cycles in significant agreement with observations (Pierini 2006; Pierini et al. 2009). In addition, its computational cost is limited compared to OGCMs. This makes such a model an ideal tool to implement the complex mathematical procedure developed in the present study to investigate the effects of singular-vector-type initial errors on the short-range prediction of the KE. Of course, the results might be model dependent and result from some deficiencies of the model dynamics. The next step will be to perform an analogous predictability analysis and related ensemble prediction experiments of the KE using an OGCM.

Although we have successfully validated the hypothesis that the linear processes play a dominant role in the error growth during the period of 180 days, we also noted that there exist some differences between the linear and nonlinear evolutions of the SV errors (Fig. 9), which suggests that nonlinearity may play a role in the error evolutions. The role of nonlinearity will be analyzed in detail in a future model study.

Acknowledgments. The authors thank three anonymous reviewers for their valuable comments. This study was supported by the National Natural Scientific Foundation of China (41576015, 41306023, 41490644, and 41490640), the NSFC Innovative Group Grant (41421005), the NSFC-Shandong Joint Fund for Marine Science Research Centers (U1406401), the National Programme on Global Change and Air-Sea Interaction (GASI-IPOVAI-06), and the Natural Sciences and Engineering Research Council (NSERC) of Canada Discovery Grant to Y. Tang. S. Pierini acknowledges support from the University of Naples Parthenope (Contracts DSTE315 and DSTE254).

APPENDIX

Derivation of the Evolution Equation for the Perturbation Kinetic Energy

The evolution of the perturbation kinetic energy defined in Eq. (11) can be written as follows:

$$\frac{\partial E'_{K,g}(t)}{\partial t} = (h_b + \eta')\frac{\partial\{[(u')^2 + (v')^2]/2\}}{\partial t} + \frac{1}{2}[(u')^2 + (v')^2]\frac{\partial(h_b + \eta')}{\partial t}, \quad \text{(A1)}$$

where the subscript b denotes the values of the background states.

For convenience, we define

$$\Pi = \frac{1}{2}[(u')^2 + (v')^2], \quad \text{and} \quad H = h_b + \eta'. \quad \text{(A2)}$$

To obtain the evolution equations of perturbation (u', v'), we substitute $(u_b + u', v_b + v', \eta_b + \eta)$ and (u_b, v_b, η_b) into Eqs. (1a) and (1b), respectively, and obtain two equations, whose difference gives the following:

$$\frac{\partial u'}{\partial t} + (u_b + u')\frac{\partial u'}{\partial x} + (v_b + v')\frac{\partial u'}{\partial y} + u'\frac{\partial u_b}{\partial x} + v'\frac{\partial u_b}{\partial y} - fv' = -g'\frac{\partial \eta'}{\partial x} + A_H\nabla^2 u' - \gamma(u_b + u')\sqrt{(u_b + u')^2 + (v_b + v')^2} + \gamma u_b\sqrt{u_b^2 + v_b^2} + \frac{\tau}{\rho H} - \frac{\tau}{\rho h_b}, \quad \text{and} \quad \text{(A3)}$$

$$\frac{\partial v'}{\partial t} + (u_b + u')\frac{\partial v'}{\partial x} + (v_b + v')\frac{\partial v'}{\partial y} + u'\frac{\partial v_b}{\partial x} + v'\frac{\partial v_b}{\partial y} + fu' = -g'\frac{\partial \eta'}{\partial y} + A_H\nabla^2 v' - \gamma(v_b + v')\sqrt{(u_b + u')^2 + (v_b + v')^2} + \gamma v_b\sqrt{u_b^2 + v_b^2}. \quad \text{(A4)}$$

If we multiply Eqs. (A3) and (A4) by u' and v', respectively, and then add the equations, we get the following:

$$\frac{\partial \Pi}{\partial t}+(u_b+u')\frac{\partial \Pi}{\partial x}+(v_b+v')\frac{\partial \Pi}{\partial y}+\left(u'u'\frac{\partial u_b}{\partial x}+u'v'\frac{\partial u_b}{\partial y}+u'v'\frac{\partial v_b}{\partial x}+v'v'\frac{\partial v_b}{\partial y}\right)$$
$$=-g'\left(u'\frac{\partial \eta'}{\partial x}+v'\frac{\partial \eta'}{\partial y}\right)+A_H(u'\nabla^2u'+v'\nabla^2v')-\gamma[(u_b+u')u'+(v_b+v')v']\sqrt{(u_b+u')^2+(v_b+v')^2}$$
$$+\gamma(u_bu'+v_bv')\sqrt{u_b^2+v_b^2}+u'\left(\frac{\tau}{\rho H}-\frac{\tau}{\rho h_b}\right). \tag{A5}$$

On the other hand, according to Eq. (1c), we can get the following equation for H:

$$\frac{\partial H}{\partial t}=-\left[(u_b+u')\frac{\partial H}{\partial x}+(v_b+v')\frac{\partial H}{\partial y}+H\frac{\partial (u_b+u')}{\partial x}+H\frac{\partial (v_b+v')}{\partial y}\right]. \tag{A6}$$

Substituting Eqs. (A5) and (A6) into Eq. (A1) and then rearranging, we get

$$\frac{\partial E'_{K,g}(t)}{\partial t}=H\frac{\partial \Pi}{\partial t}+\Pi\frac{\partial H}{\partial t}$$
$$=\mathrm{ADV}+\mathrm{BT}+\mathrm{DIV}+\mathrm{VF}+\mathrm{WIND}. \tag{A7}$$

In Eq. (A7), the expression of each term is

$$\mathrm{ADV}=-(u_b+u')\frac{\partial E'_{K,g}}{\partial x}-(v_b+v')\frac{\partial E'_{K,g}}{\partial y}$$
$$-g'(h_b+\eta')\left(u'\frac{\partial \eta'}{\partial x}+v'\frac{\partial \eta'}{\partial y}\right), \tag{A8}$$

$$\mathrm{BT}=-(h_b+\eta')\left[\left(\frac{3}{2}u'u'+\frac{1}{2}v'v'\right)\frac{\partial u_b}{\partial x}+u'v'\frac{\partial u_b}{\partial y}+u'v'\frac{\partial v_b}{\partial x}+\left(\frac{1}{2}u'u'+\frac{3}{2}v'v'\right)\frac{\partial v_b}{\partial y}\right], \tag{A9}$$

$$\mathrm{DIV}=-\frac{u'u'+v'v'}{2}(h_b+\eta')\left(\frac{\partial u'}{\partial x}+\frac{\partial v'}{\partial y}\right), \tag{A10}$$

$$\mathrm{VF}=A_H(h_b+\eta')(u'\nabla^2u'+v'\nabla^2v')-\gamma(h_b+\eta')$$
$$\times[u'(u_b+u')+v'(v_b+v')]\sqrt{(u_b+u')^2+(v_b+v')^2}$$
$$+\gamma(h_b+\eta')(u_bu'+v_bv')\sqrt{u_b^2+v_b^2}, \tag{A11}$$

and

$$\mathrm{WIND}=u'(h_b+\eta')\left[\frac{\tau}{\rho(h_b+\eta')}-\frac{\tau}{\rho h_b}\right]. \tag{A12}$$

We have discussed each term in section 4b. By diagnosing the contribution of each term, the dominant physical process responsible for the error growth can be revealed.

REFERENCES

Buizza, R., and T. N. Palmer, 1995: The singular vector structure of the atmosphere global circulation. *J. Atmos. Sci.*, **52**, 1434–1456, doi:10.1175/1520-0469(1995)052<1434:TSVSOT>2.0.CO;2.

Dijkstra, H. A., and M. Ghil, 2005: Low-frequency variability of the large-scale ocean circulation: A dynamical systems approach. *Rev. Geophys.*, **43**, RG3002, doi:10.1029/2002RG000122.

Douglass, E. M., S. R. Jayne, F. O. Bryan, S. Peacock, and M. Maltrud, 2012: Kuroshio pathways in a climatologically forced model. *J. Oceanogr.*, **68**, 625–639, doi:10.1007/s10872-012-0123-y.

Ehrendorfer, M., and J. J. Tribbia, 1997: Optimal prediction of forecast error covariances through singular vectors. *J. Atmos. Sci.*, **54**, 286–313, doi:10.1175/1520-0469(1997)054<0286:OPOFEC>2.0.CO;2.

Farrell, B. F., 1990: Small error dynamics and the predictability of flows. *J. Atmos. Sci.*, **47**, 2409–2416, doi:10.1175/1520-0469(1990)047<2409:SEDATP>2.0.CO;2.

Frankignoul, C., N. Sennechael, Y.-O. Kwon, and M. A. Alexander, 2011: Influence of the meridional shifts of the Kuroshio and the Oyashio Extensions on the atmospheric circulation. *J. Climate*, **24**, 762–777, doi:10.1175/2010JCLI3731.1.

Fujii, Y., H. Tsujino, N. Usui, H. Nakano, and M. Kamachi, 2008: Application of singular vector analysis to the Kuroshio large meander. *J. Geophys. Res.*, **113**, C07026, doi:10.1029/2007JC004476.

Hawkins, E. D., and R. Sutton, 2011: Estimating climatically relevant singular vectors for decadal predictions of the Atlantic Ocean. *J. Climate*, **24**, 109–123, doi:10.1175/2010JCLI3579.1.

Islam, S. U., Y. Tang, and P. L. Jackson, 2016: Optimal error growth of South Asian monsoon forecast associated with the uncertainties in the sea surface temperature. *Climate Dyn.*, **46**, 1953–1975, doi:10.1007/s00382-015-2686-y.

Kelly, K. A., R. J. Small, R. M. Samelson, B. Qiu, T. M. Joyce, Y. Kwon, and M. F. Cronin, 2010: Western boundary currents and frontal air–sea interaction: Gulf Stream and Kuroshio Extension. *J. Climate*, **23**, 5644–5667, doi:10.1175/2010JCLI3346.1.

Kleeman, R., Y. Tang, and A. M. Moore, 2003: The calculation of climatically relevant singular vectors in the presence of weather noise as applied to the ENSO problem. *J. Atmos. Sci.*, **60**, 2856–2868, doi:10.1175/1520-0469(2003)060<2856:TCOCRS>2.0.CO;2.

Kramer, W., H. A. Dijkstra, S. Pierini, and P. J. van Leeuwen, 2012: Measuring the impact of observations on the predictability of the Kuroshio Extension in a shallow-water model. *J. Phys. Oceanogr.*, **42**, 3–17, doi:10.1175/JPO-D-11-014.1.

Kurogi, M., H. Hasumi, and Y. Tanaka, 2013: Effects of stretching on maintaining the Kuroshio meander. *J. Geophys. Res. Oceans*, **118**, 1182–1194, doi:10.1002/jgrc.20123.

Kwon, Y.-O., and T. M. Joyce, 2013: Northern Hemisphere winter atmospheric transient eddy heat fluxes and the Gulf Stream and Kuroshio–Oyashio Extension variability. *J. Climate*, **26**, 9839–9859, doi:10.1175/JCLI-D-12-00647.1.

Miyazawa, Y., X. Guo, and T. Yamagata, 2004: Roles of mesoscale eddies in the Kuroshio paths. *J. Phys. Oceanogr.*, **34**, 2203–2222, doi:10.1175/1520-0485(2004)034<2203:ROMEIT>2.0.CO;2.

Moore, A. M., and A. J. Mariano, 1999: The dynamics of error growth and predictability in a model of the Gulf Stream. Part I: Singular vector analysis. *J. Phys. Oceanogr.*, **29**, 158–176, doi:10.1175/1520-0485(1999)029<0158:TDOEGA>2.0.CO;2.

Mu, M., W. Duan, and B. Wang, 2007: Season-dependent dynamics of nonlinear optimal error growth and El Niño-Southern Oscillation predictability in a theoretical model. *J. Geophys. Res.*, **112**, D10113, doi:10.1029/2005JD006981.

Nishikawa, H., I. Yasuda, and S. Itoh, 2011: Impact of winter-to-spring environmental variability along the Kuroshio jet on the recruitment of Japanese sardine. *Fish. Oceanogr.*, **20**, 570–582, doi:10.1111/j.1365-2419.2011.00603.x.

Nonaka, M., H. Nakamura, Y. Tanimoto, T. Kagimoto, and H. Sasaki, 2006: Decadal variability in the Kuroshio–Oyashio Extension simulated in an eddy-resolving OGCM. *J. Climate*, **19**, 1970–1989, doi:10.1175/JCLI3793.1.

——, H. Sasaki, B. Taguchi, and H. Nakamura, 2012: Potential predictability of interannual variability in the Kuroshio Extension jet speed in an eddy-resolving OGCM. *J. Climate*, **25**, 3645–3652, doi:10.1175/JCLI-D-11-00641.1.

——, Y. Sasai, H. Sasaki, B. Taguchi, and H. Nakamura, 2016: How potentially predictable are midlatitude ocean currents? *Sci. Rep.*, **6**, 20153, doi:10.1038/srep20153.

O'Reilly, C. H., and A. Czaja, 2015: The response of the Pacific storm track and atmospheric circulation to Kuroshio Extension variability. *Quart. J. Roy. Meteor. Soc.*, **141**, 52–66, doi:10.1002/qj.2334.

Pierini, S., 2006: A Kuroshio Extension system model study: Decadal chaotic self-sustained oscillations. *J. Phys. Oceanogr.*, **36**, 1605–1625, doi:10.1175/JPO2931.1.

——, 2008: On the crucial role of basin geometry in double-gyre models of the Kuroshio Extension. *J. Phys. Oceanogr.*, **38**, 1327–1333, doi:10.1175/2007JPO3924.1.

——, 2010: Coherence resonance in a double-gyre model of the Kuroshio Extension. *J. Phys. Oceanogr.*, **40**, 238–248, doi:10.1175/2009JPO4229.1.

——, 2014: Kuroshio Extension bimodality and the North Pacific Oscillation: A case of intrinsic variability paced by external forcing. *J. Climate*, **27**, 448–454, doi:10.1175/JCLI-D-13-00306.1.

——, 2015: A comparative analysis of Kuroshio Extension indices from a modeling perspective. *J. Climate*, **28**, 5873–5881, doi:10.1175/JCLI-D-15-0023.1.

——, H. A. Dijkstra, and A. Riccio, 2009: A nonlinear theory of the Kuroshio Extension bimodality. *J. Phys. Oceanogr.*, **39**, 2212–2229, doi:10.1175/2009JPO4181.1.

——, ——, and M. Mu, 2014: Intrinsic low-frequency variability and predictability of the Kuroshio Current and of its extension. *Adv. Oceanol. Limnol.*, **5**, 1–44, doi:10.4081/aiol.2014.5348.

Qiu, B., 2000: Interannual variability of the Kuroshio Extension system and its impact on the wintertime SST field. *J. Phys. Oceanogr.*, **30**, 1486–1502, doi:10.1175/1520-0485(2000)030<1486:IVOTKE>2.0.CO;2.

——, 2002: The Kuroshio Extension system: Its large-scale variability and role in the midlatitude ocean–atmosphere interaction. *J. Oceanogr.*, **58**, 57–75, doi:10.1023/A:1015824717293.

——, 2003: Kuroshio Extension variability and forcing of the Pacific decadal oscillations: Responses and potential feedback. *J. Phys. Oceanogr.*, **33**, 2465–2482, doi:10.1175/2459.1.

——, and S. Chen, 2005: Variability of the Kuroshio Extension jet, recirculation gyre, and mesoscale eddies on decadal time scales. *J. Phys. Oceanogr.*, **35**, 2090–2103, doi:10.1175/JPO2807.1.

——, and ——, 2010: Eddy-mean flow interaction in the decadally modulating Kuroshio Extension system. *Deep-Sea Res. II*, **57**, 1098–1110, doi:10.1016/j.dsr2.2008.11.036.

——, ——, N. Schneider, and B. Taguchi, 2014: A coupled decadal prediction of the dynamic state of the Kuroshio Extension system. *J. Climate*, **27**, 1751–1764, doi:10.1175/JCLI-D-13-00318.1.

Schmeits, M. J., and H. A. Dijkstra, 2001: Bimodal behavior of the Kuroshio and the Gulf Stream. *J. Phys. Oceanogr.*, **31**, 3435–3456, doi:10.1175/1520-0485(2001)031<3435:BBOTKA>2.0.CO;2.

Seager, R., Y. Kushnir, N. H. Naik, M. A. Cane, and J. Miller, 2001: Wind-driven shifts in the latitude of the Kuroshio–Oyashio Extension and generation of SST anomalies on decadal timescales. *J. Climate*, **14**, 4249–4265, doi:10.1175/1520-0442(2001)014<4249:WDSITL>2.0.CO;2.

Seo, Y., S. Sugimoto, and K. Hanawa, 2014: Long-term variations of the Kuroshio Extension path in winter: Meridional movement and path state change. *J. Climate*, **27**, 5929–5940, doi:10.1175/JCLI-D-13-00641.1.

Simmons, A. J., R. Mureau, and T. Petroliagis, 1995: Error growth and estimates of predictability from the ECMWF forecasting system. *Quart. J. Roy. Meteor. Soc.*, **121**, 1739–1771, doi:10.1002/qj.49712152711.

Sugimoto, S., and K. Hanawa, 2012: Relationship between the path of the Kuroshio in the south of Japan and the path of the Kuroshio Extension in the east. *J. Oceanogr.*, **68**, 219–225, doi:10.1007/s10872-011-0089-1.

Taguchi, B., S.-P. Xie, N. Schneider, M. Nonaka, H. Sasaki, and Y. Sasai, 2007: Decadal variability of the Kuroshio Extension: Observations and an eddy-resolving model hindcast. *J. Climate*, **20**, 2357–2377, doi:10.1175/JCLI4142.1.

——, B. Qiu, M. Nonaka, H. Sasaki, S.-P. Xie, and N. Schneider, 2010: Decadal variability of the Kuroshio Extension: Mesoscale eddies and recirculation. *Ocean Dyn.*, **60**, 673–691, doi:10.1007/s10236-010-0295-1.

Tang, Y., R. Kleeman, and S. Miller, 2006: ENSO predictability of a fully coupled GCM model using singular vector analysis. *J. Climate*, **19**, 3361–3377, doi:10.1175/JCLI3771.1.

Tokinaga, H., Y. Tanimoto, S.-P. Xie, T. Sampe, H. Tomita, and H. Ichikawa, 2009: Ocean frontal effects on the vertical development on clouds over the western North Pacific: In situ and satellite observations. *J. Climate*, **22**, 4241–4260, doi:10.1175/2009JCLI2763.1.

Tsujino, H., N. Usui, and H. Nakano, 2006: Dynamics of Kuroshio path variations in a high-resolution general circulation model. *J. Geophys. Res.*, **111**, C11001, doi:10.1029/2005JC003118.

Usui, N., H. Tsujino, H. Nakano, and Y. Fujii, 2008: Formation process of the Kuroshio large meander in 2004. *J. Geophys. Res.*, **113**, C08047, doi:10.1029/2008JE003225.

Wang, S., Z. Liu, C. Pang, and H. Liu, 2016: The decadally modulating eddy field in the upstream Kuroshio Extension and its related mechanisms. *Acta Oceanol. Sin.*, **35**, 9–17, doi:10.1007/s13131-015-0741-5.